JGR Atmospheres

RESEARCH ARTICLE
10.1029/2020JD032866

First Lidar Observations of Quasi-Biennial Oscillation-Induced Interannual Variations of Gravity Wave Potential Energy Density at McMurdo via a Modulation of the Antarctic Polar Vortex

Zimu Li[1,2], Xinzhao Chu[2], V. Lynn Harvey[3], Jackson Jandreau[2], Xian Lu[4], Zhibin Yu[2,5], Jian Zhao[2], and Weichun Fong[2]

[1]School of Earth and Space Sciences, University of Science and Technology of China, Hefei, China, [2]Cooperative Institute of Research in Environmental Sciences and Department of Aerospace Engineering Sciences, University of Colorado Boulder, Boulder, CO, USA, [3]Laboratory for Atmosphere and Space Physics, University of Colorado Boulder, Boulder, CO, USA, [4]Department of Physics and Astronomy, Clemson University, Clemson, SC, USA, [5]Harbin Institute of Technology (Shenzhen), Shenzhen, China

Key Points:
- We report a Quasi-Biennial Oscillation in Antarctic gravity wave activity—potential energy density is enhanced during QBO easterly winters
- Antarctic polar vortex edge moves equatorward/poleward during QBO easterly/westerly phases with a maximum latitude difference of ~8° in June
- An equatorward shifted polar vortex corresponds to less critical level filtering of gravity waves and thus higher E_{pm} in QBO easterly winters

Correspondence to:
X. Chu,
xinzhao.chu@colorado.edu

Citation:
Li, Z., Chu, X., Harvey, V. L., Jandreau, J., Lu, X., Yu, Z., et al. (2020). First lidar observations of Quasi-Biennial Oscillation-induced interannual variations of gravity wave potential energy density at McMurdo via a modulation of the Antarctic polar vortex. *Journal of Geophysical Research: Atmospheres*, *125*, e2020JD032866. https://doi.org/10.1029/2020JD032866

Received 1 APR 2020
Accepted 6 JUL 2020
Accepted article online 26 JUL 2020

Author Contributions:
Conceptualization: Xinzhao Chu
Data curation: Zimu Li, Xinzhao Chu, Zhibin Yu, Jian Zhao, Weichun Fong
Formal analysis: Zimu Li, Xinzhao Chu, V. Lynn Harvey, Jackson Jandreau
Investigation: Zimu Li, Xinzhao Chu, V. Lynn Harvey, Jackson Jandreau, Zhibin Yu
Methodology: Zimu Li, Xinzhao Chu, V. Lynn Harvey, Xian Lu
Software: Zimu Li, V. Lynn Harvey, Jackson Jandreau, Jian Zhao, Weichun Fong
Validation: Zimu Li, Xinzhao Chu, V. Lynn Harvey, Jackson Jandreau
Writing - original draft: Xinzhao Chu
(continued)

Abstract This work presents the first lidar observations of a Quasi-Biennial Oscillation (QBO) in the interannual variations of stratospheric gravity wave potential energy density (E_{pm} in 30–50 km) at McMurdo (77.84°S, 166.67°E), Antarctica. This paper also reports the first identification of QBO signals in the distance between McMurdo and the polar vortex edge. Midwinter stratospheric gravity wave activity is stronger during the QBO easterly phase when the June polar vortex expands and the polar night jet shifts equatorward. During the QBO westerly phase, gravity wave activity is weaker when the polar vortex contracts and the polar night jet moves poleward. Nine years of lidar data (2011–2019) exhibit the mean E_{pm} winter maxima being ~43% higher during QBO easterly than westerly. The June polar vortex edge at 45 km altitude moves equatorward/poleward during QBO easterly/westerly phases with ~8° latitude differences (39.7°S vs. 47.7°S) as revealed in 21 years of MERRA-2 data (1999–2019). We hypothesize that an equatorward shifted polar vortex corresponds to less critical level filtering of gravity waves and thus higher E_{pm} at McMurdo. The critical level filtering is characterized by wind rotation angle (WRA), and we find a linear correlation between the WRA and E_{pm} interannual variations. The results suggest that the QBO is likely controlling the interannual variations of the E_{pm} winter maxima over McMurdo via the critical level filtering. This observationally based study lays the groundwork for a rigorous numerical study that will provide robust statistics to better understand the mechanisms that link the tropical QBO to extratropical waves.

1. Introduction

Atmospheric waves, such as gravity, tidal, and planetary waves, transport momentum and energy both vertically and horizontally, making significant contributions to the complex coupling among stratified layers from the troposphere to the thermosphere, between the Northern and Southern Hemispheres, and crossing over the polar, middle, and equatorial regions (e.g., Andrews et al., 1987; Becker, 2012, 2017; Forbes, 1995; Smith, 2012a, 2012b). Insufficient and inaccurate representation of gravity waves remains one of the leading errors in most general circulation models and chemical climate models (e.g., Alexander et al., 2010; Garcia et al., 2014, 2017; Geller et al., 2013; Kim et al., 2003; Liu, 2019; McLandress et al., 2006; Richter et al., 2010), because, due to their small scales and wide spectra, it is still very challenging to characterize gravity waves with observations and provide the physical basis for wave parameterizations and simulations. The McMurdo lidar campaign conducted by the University of Colorado Boulder was designed to help address this challenge by making high-resolution, full diurnal cycle, and all-year-round observations at a very high southern latitude of ~78°S (Chu, Huang, et al., 2011; Chu, Yu, et al., 2011). This ongoing campaign has collected data for the last decade since late 2010. The lidar data have revealed McMurdo as a geophysical hot spot of atmospheric waves (e.g., Chen et al., 2013, 2016; Chen & Chu, 2017; Chu, Huang, et al., 2011; Chu, Yu, et al., 2011; Chu et al., 2018; Lu et al., 2015, 2017; Zhao et al., 2017), and the discovery of persistent gravity waves in the

Writing – review & editing: Zimu Li, Xinzhao Chu, V. Lynn Harvey, Jackson Jandreau, Xian Lu, Zhibin Yu

mesosphere and lower thermosphere (MLT) (Chen et al., 2016) have inspired systematic studies of gravity waves from the thermosphere to the stratosphere in Antarctica.

Much has been learned about short-term gravity wave variations over McMurdo. For example, lidar observations reveal thermosphere-ionosphere Fe (TIFe) layers with clear gravity wave signatures (periods ~1.5 hr) to at least 170 km in altitude (Chu, Yu, et al., 2011; Chu et al., 2016; Chu & Yu, 2017). Such 1.5–2 hr gravity waves have vertical wavelengths varying from ~ 20 km to over 70 km into the thermosphere (Chen, 2016; Chu, Yu, et al., 2011; Chu et al., 2012). Gravity waves with periods of 3–10 hr dominate the temperature perturbations in the MLT in such paramount ways (Chen et al., 2016; Chen & Chu, 2017) that no tidal signatures can be seen without averaging over several years of lidar data (Fong et al., 2014). Consequently, Chen et al. (2016) named these MLT waves the "persistent gravity waves." Case studies of the persistent waves point their sources to the stratosphere (Chen et al., 2013). Studies of stratospheric gravity waves using 5 years of Fe lidar data from 2011 to 2015 exhibit a repeated seasonal pattern with summer minima and winter maxima in the gravity wave potential energy mass density (E_{pm}) between 30 and 50 km (Chu et al., 2018) and the seasonal variations in the wave periods and vertical wavelengths of stratospheric dominant gravity waves (Zhao et al., 2017). Chu et al. (2018) have found that the summer-winter asymmetry in the E_{pm} variations are mainly caused by the critical level filtering, while the E_{pm} variations during winter months are positively correlated with the near-surface and stratospheric winds. The derived horizontal wavelengths (~400 km) of dominant gravity waves in the stratosphere (Zhao et al., 2017) are significantly shorter than those (~2,000 km) of the persistent gravity waves in the MLT (Chen et al., 2013; Chen & Chu, 2017), leading to the conclusion that dominant gravity waves in the stratosphere are starkly different from the large-scale persistent gravity waves in the MLT. Combining the McMurdo lidar observations (Chen et al., 2013, 2016; Chen & Chu, 2017; Chu et al., 2018; Zhao et al., 2017) with Kühlungsborn Mechanistic general Circulation Model (KMCM) numerical simulations (Becker & Vadas, 2018; Vadas & Becker, 2018) and updating the original theory of secondary gravity wave generation (Vadas et al., 2003), Vadas et al. (2018) proposed a "primary-secondary" wave coupling picture in Antarctica to reconcile the observed large differences between the MLT and the stratospheric gravity waves. That is, the downslope winds blowing down from the East Antarctic plateau onto the Ross Sea generate orographic gravity waves with considerably large amplitudes. As these orographic gravity waves dissipate near the stratopause or in the lower mesosphere, momentum deposition results in localized and intermittent body forces. Such body forces excite the secondary gravity waves that possess scales several times larger than the primary orographic gravity waves (Vadas et al., 2018). These large-scale secondary gravity waves can propagate and penetrate to the lower thermosphere, forming the persistent gravity waves. The secondary gravity wave signatures predicted by the theory in Vadas et al. (2018) were successfully identified in the McMurdo lidar data (Vadas et al., 2018) and in the KMCM simulations (Vadas & Becker, 2018).

Despite the above picture being quite complete in terms of short-term variations and vertical coupling by gravity waves in Antarctica, there remain important unanswered questions concerning long-term variations and horizontal coupling. For example, we still do not know what factors drive the interannual variations in the observed gravity wave E_{pm}. Chu et al. (2018) have noted from the 5 years of data that the stratospheric E_{pm} shows larger winter values in 2012 and 2015 than in the other three years (2011, 2013, and 2014) and suggested that the critical level filtering may play a role; however, the causes and mechanisms remained unresolved. Now we have learned that 2012 and 2015 correspond to the easterly phase of the equatorial Quasi-Biennial Oscillation (QBO), while the other three years are in the westerly phase. Is the equatorial QBO responsible for the interannual variations of polar gravity waves? Signatures of the QBO at high latitudes have been observed since the 1960s following the discovery of the tropical oscillation (see a review by Anstey & Shepherd, 2014), and Holton and Tan (1980) proposed a mechanism, often referred to as the Holton-Tan effect, to explain the dynamical coupling between low and high latitudes. It is known that QBO can affect the polar wind and temperature fields including the Antarctic (e.g., Baldwin & Dunkerton, 1998; Ford et al., 2009; Lu et al., 2019; Yamashita et al., 2018) and that background winds impact gravity waves substantially (e.g., Becker, 2012; Fritts & Alexander, 2003); therefore, it is plausible that the tropical QBO affects the very high latitude gravity wave activity. This clue leads us to investigate the interannual variations of E_{pm} and their correlation with the QBO as Part 3 of our studies of stratospheric gravity waves at McMurdo, following Part 1 (dominant gravity wave characteristics and their seasonal variations) in Zhao et al. (2017) and Part 2 (gravity wave potential energy densities and their seasonal variations) in

Table 1
Statistics of Qualified Lidar Data (in Hours) for Individual Months From 2011 to 2019

	2011	2012	2013	2014	2015	2016	2017	2018	2019	Total
Jan	82	108	90	160	61	121	151	16	100	889
Feb	85	95	19	41	51	144	67	36	104	642
Mar	36	19	49	54	57	58	23	30	77	403
Apr	40	26	99	30	52	102	24	34	91	498
May	59	53	45	126	66	41	60	80	52	582
Jun	72	72	71	104	121	44	30	0	42	556
Jul	54	21	83	79	104	81	54	33	155	664
Aug	67	26	63	34	42	11	51	42	115	451
Sep	14	49	47	31	67	23	32	6	31	300
Oct	38	98	53	82	48	8	12	25	82	446
Nov	148	96	91	50	14	0	99	165	51	714
Dec	160	49	206	130	81	63	53	178	78	998
Total	855	712	916	921	764	696	656	645	978	7,143

Chu et al. (2018). With the aid of 21 years (1999–2019) of reanalysis data from the Modern Era Retrospective Analysis of Research and Applications, Version 2 (MERRA-2; Bosilovich et al., 2015), we find in this study that the Antarctic polar vortex edge exhibits an equatorward shift corresponding to the enhanced gravity wave E_{pm} in QBO easterly June. Based on the results, we will propose an explanation for how the equatorial QBO may impact the polar gravity waves. This observational study lays the groundwork for future numerical studies that will provide more robust statistics to better understand the mechanisms that link the tropical QBO to extratropical gravity waves.

2. McMurdo Lidar Observations, MERRA-2 Reanalysis Data, and Methodology

2.1. Lidar Observational Campaign at Arrival Heights

The McMurdo lidar observation campaigns have been conducted by the University of Colorado Boulder at Arrival Heights Observatory via collaboration between the United States Antarctic Program (USAP) and the Antarctica New Zealand (AntNZ) for nearly a decade. The first Fe Boltzmann lidar (Chu et al., 2002) was installed in the AntNZ Arrival Heights building and started the data collection in December 2010 (Chu, Huang, et al., 2011; Chu, Yu, et al., 2011). Seven years later the second lidar, a STAR Na Doppler lidar (Smith & Chu, 2015), was added to the same lidar lab, and simultaneous Fe and Na lidar data have been collected since January 2018. Nine years of Fe lidar data are chosen for this study because of their longer records than the Na lidar. Atmospheric temperature profiles are derived using the Rayleigh integration technique in the pure molecular scattering region (Hauchecorne & Chanin, 1980) and using the Fe Boltzmann technique in the meteoric Fe layer region (Chu et al., 2002; Gelbwachs, 1994). The raw photon counts of Fe lidar were collected in resolutions of 1 min and 48 m. To achieve sufficient signal-to-noise ratios (SNRs), we take the same methodology as in Chu et al. (2018); that is, the Rayleigh temperature data were retrieved with a temporal integration window of 2 hr and a spatial binning window of 0.96 km, and an oversampling method was applied to have steps of 1 hr and 0.96 km.

Over the course of 9 years (2011–2019), more than 9,000 hr of Fe lidar data were collected from Arrival Heights Observatory. Comprehensive data screening similar to that in Chu et al. (2018) and Zhao et al. (2017) removed data that have durations less than 6 hr or large temporal gaps (≥4 hr), or low SNRs (Zhao et al., 2017). Consequently, 7,143 hr of data qualify for this study. Statistics of the qualified lidar data are tabulated in Table 1. Qualified data further went through a data division process as described in Zhao et al. (2017) to create data segments between 6 and 12 hr in duration. As pointed out by Chu et al. (2018), segmenting the data in this way enriches statistical samples while preserving the persistent gravity waves with periods of 3–10 hr that are the dominant features in the temperature variations at McMurdo (Chen et al., 2016; Zhao et al., 2017). There are 646 total segments, and their distributions are listed in Table 2. All months, except for June 2018 and November 2016, have acquired qualified data samples for gravity wave

Table 2
Comparison of Qualified Lidar Data Segments From 2011 to 2019

	Segment number									
	2011	2012	2013	2014	2015	2016	2017	2018	2019	Total
Jan	8	11	8	6	6	11	15	2	10	77
Feb	7	9	1	4	4	13	7	3	10	58
Mar	3	2	4	4	5	5	2	3	7	35
Apr	4	2	8	4	6	9	4	3	8	48
May	6	4	5	11	7	4	5	7	5	54
Jun	6	6	6	10	12	4	3	0	4	51
Jul	4	2	7	8	9	7	5	3	14	59
Aug	6	2	5	4	4	1	5	5	10	42
Sep	1	6	5	3	7	2	3	1	3	31
Oct	3	8	5	8	5	1	1	3	8	42
Nov	14	8	9	5	1	0	9	14	5	65
Dec	13	5	13	12	7	6	5	16	7	84
Total	75	65	76	79	73	63	64	60	91	646

studies. After the data screening and division process, the actual data used in this study total to ~6,941 hr, and their distributions of segment lengths and hours are summarized in Table 3.

About 70% of the segments have durations longer than 10 hr, and the short duration segments (6 hr) account for only ~5%. The data segmenting and the subsequent processing with background subtraction and spectral filtering, as outlined in Chu et al. (2018), indicates that gravity waves with periods of 3–9 hr and vertical wavelengths of 2–20 km are the major contributors to the derived gravity wave E_{pm}, while gravity waves with periods of 9–11 hr and vertical wavelengths of 20–30 km contribute partial energy to the E_{pm}. The 3 dB cutoff period and vertical wavelength are 11 hr and 30 km for the temporal and spatial filters used in the data processing. Such filters are set to preserve the persistent gravity wave spectra (Chen et al., 2013, 2016; Chen & Chu, 2017) as fully as possible while significantly removing semidiurnal tides, diurnal tides, and planetary wave components with periods over 1 day and vertical wavelengths over 40 km that are dominant in the stratosphere (Lu et al., 2013, 2017). As studied in Part 1 (Zhao et al., 2017), the dominant gravity waves in the stratosphere have similar periods (3–10 hr) as the persistent gravity waves in the MLT but with much shorter vertical wavelengths (3–16 km), and the mean wave periods and vertical wavelengths in the stratosphere vary from ~4.5 hr and ~5.5 km in summer to ~6 hr and ~8.5 km in winter. Detailed analysis of how the data processing and segmenting procedure affects gravity wave spectra and how the aforementioned spectral ranges are reached can be found in section 2.2.1 of Chu et al. (2018).

2.2. Derivations of E_{pm} and E_{pv} From Lidar Data

Two main physical quantities used in this study are the gravity wave potential energy per unit mass (E_{pm}, potential energy mass density) and potential energy per unit volume (E_{pv}, potential energy volume density). We use the same method as Chu et al. (2018) to calculate the altitude profile of $E_{pm}(Z)$

Table 3
Statistics on Observational Segments From 2011 to 2019 Employed in the Study

Data duration	Total	12 hr	11 hr	10 hr	9 hr	8 hr	7 hr	6 hr
Number of segments	646	410	43	36	42	37	46	32
Percentage	100.00%	63.47%	6.66%	5.57%	6.50%	5.73%	7.12%	4.95%
Number of hours	6,941	4,920	473	360	378	296	322	192
Percentage	100.00%	70.88%	6.81%	5.19%	5.45%	4.26%	4.64%	2.77%

$$E_{pm}(z) = \frac{1}{2}\overline{\frac{g^2}{N^2(z)}\left(\frac{T'_{GW}(z,\,t)}{T_{Bkg}(z)}\right)^2} = \frac{1}{2}\overline{\frac{g^2}{N^2(z)}}\frac{1}{n_p}\sum_{i=1}^{n_p}\left(\frac{T'_{GW}(z,t_i)}{T_{Bkg}(z)}\right)^2 \quad (1)$$

where the overbar denotes taking the mean over the time span of the observational segment, the gravitational acceleration $g = 9.7$ m/s^2 corresponding to the stratosphere, z and t respectively represent altitude and time, T_{Bkg} is the monthly mean background temperature, T'_{GW} represents the pure temperature perturbations induced by gravity waves, and n_p is the number of temperature perturbation profiles within the segment time span. Here $N(z)$ is the buoyancy frequency calculated from the segment temporal mean temperatures $T_0(Z)$ through

$$N^2(z) = -\frac{g}{T_0(z)}\left(\frac{dT_0(z)}{dz} + \frac{g}{C_p}\right) \quad (2)$$

where $C_p = 1{,}004$ J/K/kg is the specific heat of dry air at constant pressure. We also compute the altitude profile of $E_{pv}(z)$, for each observational segment, by multiplying $E_{pm}(z)$ with the background atmospheric density $\rho_0(z)$:

$$E_{pv}(z) = \rho_0(z)E_{pm}(z) \quad (3)$$

The procedures of deriving E_{pm} and E_{pv} from temperature profiles are quite involved, as the key steps include (1) deriving gravity wave-induced temperature perturbations from the raw temperature data, and (2) accurately estimating the energy of gravity waves from the derived perturbations (Chu et al., 2018). The major challenges are how to retain gravity wave-induced perturbations while removing the influences from other atmospheric waves (such as tides and planetary waves) and how to remove the contributions from noise variance to the total energy density. Chu et al. (2018) have done extensive investigations into these issues and provided thorough considerations and step-by-step procedures on the derivations. We closely followed the procedures outlined in section 2.2 of Chu et al. (2018), especially the background subtraction, spectral filtering, and applying the spectral proportion method to extract the potential energy density induced by gravity waves. Interested readers may refer to that article for more details.

2.3. MERRA-2 Reanalysis Data and Identification of Polar Vortex Edge

The NASA MERRA-2 reanalysis data (Bosilovich et al., 2015; Gelaro et al., 2017) provide the background temperature, zonal and meridional winds from the surface to the top boundary of 0.01 hPa (~80 km) for characterizing the QBO index, polar vortex edge distance and wind strength, and wind rotation angle (WRA). MERRA-2 produces a realistic QBO in the zonal wind, mean meridional circulation, and ozone over the 1980–2015 time period (Coy et al., 2016). This work uses reanalysis data from 1999 to 2019 due to improved data quality following the addition of AMSU-A and AMSU-B upper air radiances to the data assimilation stream in 1999 (see Figure 8 in Fujiwara et al., 2017, where AMSU stands for Advanced Microwave Sounding Unit). The inclusion of Aura Microwave Limb Sounder temperatures in August 2004 further improved the data quality above 5 hPa (40 km). The temporal, horizontal, and vertical resolutions of the MERRA-2 data used in this work are 6 hr, 0.5° latitude by 0.625° longitude, and 1–2 km, respectively.

The distance from McMurdo Station to the polar vortex edge is derived from the MERRA-2 reanalysis data. The method to demark the Antarctic vortex edge is described by Harvey et al. (2002) and briefly described here. First, the scalar field "Q" (see their Figure 1) is calculated; Q is a relative measure of strain versus rotation in the horizontal flow; it is negative where rotation dominates and is positive in regions of strong horizontal wind shear. Areas of negative Q are located inside the polar vortex, while positive Q is located at the vortex edge on the flanks of the polar night jet (PNJ) stream. The vortex edge demarcation algorithm first integrates Q around stream function contours starting in the center of the vortex and incrementing outward. Neighboring stream function contours in which line-integrated Q changes sign are saved as vortex edge "candidates." The actual vortex edge is the candidate with the fastest line-integrated wind speed. Illustrations of vortex edge location and the corresponding wind field and PNJ will be given in sections 4 and 5 (Figures 4c and 6–8). In the middle and upper stratosphere, this vortex demarcation algorithm is

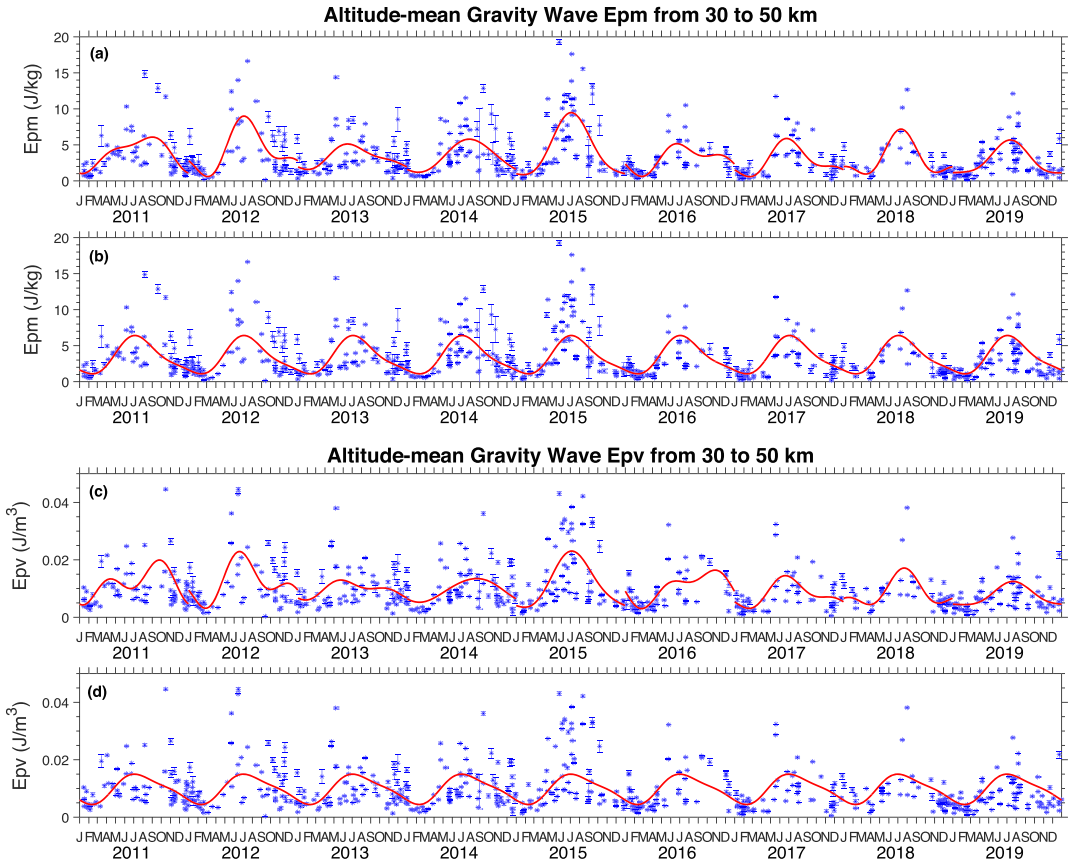

Figure 1. (a, b) Altitude mean E_{pm} (J/kg) and (c, d) altitude mean E_{pv} (J/m^3) averaged over the 30–50 km for all the qualified lidar observations over 9 years from 2011 to 2019. The blue asterisks in all panels denote the actual E_{pm} or E_{pv} values during individual observational segments with their errors shown as vertical "whiskers." The red lines are (a, c) single-year "annual + semiannual" fits for nine individual years and (b, d) uniform "annual + semiannual" fits for all years.

slightly more conservative but in good agreement (Meek et al., 2017) with the widely used "Nash" algorithm that is based on horizontal gradients in potential vorticity (Nash et al., 1996). In general, this method yields a vortex edge that is located along the poleward flank of the PNJ stream. Thus, in this work, the distance between McMurdo and the edge of the vortex can also be interpreted as the distance between McMurdo and the PNJ.

3. Interannual Variations and 9-Year Mean Annual Cycle of E_{pm}, E_{pv}, and N^2

We first explore interannual variations in 9 years of lidar data on gravity wave potential energy density averaged over the altitude range of 30 to 50 km and within each qualified data segment. Figure 1 shows the resulting 646 data points of altitude mean E_{pm} and E_{pv} versus time from 1 January 2011 to 31 December 2019. Two notable features are (1) the large fluctuations of E_{pm} and E_{pv} from one segment to another and (2) the repeated seasonal cycle showing summer minima and winter maxima. Both features are consistent with the findings studied in Chu et al. (2018) who used the first 5 years of lidar data. The goal of this work is to explain the interannual variability in the winter maxima.

To characterize the seasonal and interannual variations, the red lines in Figures 1a and 1c show nine individual harmonic fittings of annual plus semiannual oscillations, similar to that in Chu et al. (2018), for E_{pm} and E_{pv}, respectively:

Table 4
Harmonic Fitting Parameters and Errors for $\overline{E}_{pm}$ in Figures 1 and 3

Case	A_0 (J/kg)	A_{12} (J/kg)	φ_{12} (day)	A_6 (J/kg)	φ_6 (day)
Figure 1a (2011)	3.87 ± 0.29	2.20 ± 0.38	208 ± 11	0.78 ± 0.42	91 ± 14
Figure 1a (2012)	4.23 ± 0.36	3.29 ± 0.51	203 ± 10	1.69 ± 0.52	177 ± 9
Figure 1a (2013)	3.30 ± 0.27	1.54 ± 0.36	190 ± 15	0.49 ± 0.40	149 ± 21
Figure 1a (2014)	3.53 ± 0.28	2.29 ± 0.40	215 ± 10	0.14 ± 0.38	183 ± 81
Figure 1a (2015)	4.38 ± 0.42	4.26 ± 0.57	189 ± 8	0.86 ± 0.55	182 ± 21
Figure 1a (2016)	3.13 ± 0.24	1.66 ± 0.27	218 ± 13	1.00 ± 0.32	157 ± 8
Figure 1a (2017)	2.84 ± 0.24	2.16 ± 0.27	192 ± 10	1.00 ± 0.37	168 ± 8
Figure 1a (2018)	3.03 ± 0.22	2.37 ± 0.31	200 ± 8	1.29 ± 0.33	197 ± 7
Figure 1a (2019)	2.86 ± 0.29	2.26 ± 0.39	194 ± 11	0.56 ± 0.40	197 ± 23
Figure 1b (uniform)	3.47 ± 0.10	2.47 ± 0.13	199 ± 4	0.58 ± 0.15	172 ± 7
Figure 3a (composite)	3.48 ± 0.13	2.52 ± 0.18	200 ± 4	0.57 ± 0.18	172 ± 9

$$y = A_0 + A_{12}\cos\left(\frac{2\pi}{365}(x-\varphi_{12})\right) + A_6\cos\left(\frac{2\pi}{365/2}(x-\varphi_6)\right) \quad (4)$$

where A_0 is the annual mean, A_{12} and φ_{12} are the amplitude and phase of annual oscillation, and A_6 and φ_6 are the amplitude and phase of semiannual oscillation. The fitting parameters and their errors are listed in Table 4. The red curves in Figures 1b and 1d represent the uniform fittings to all years. The annual means A_0 in 2012 and 2015 are larger than the other seven years, and the amplitudes A_{12} of the annual variations in 2012, 2015, and 2018 are larger than in the other six years. The accumulated effects of larger annual means and larger annual amplitudes in the years with a QBO easterly phase are reflected in the fitted $E_{\rm pm}$ curves (see Figure 1a) that show higher midwinter maxima in 2012, 2015, and 2018 than the other years.

To quantify the interannual variations of the $E_{\rm pm}$ winter maxima occurring around the beginning of July, we take the monthly means in June and July from the nine individual annual fittings for comparison. The mean of all 18 monthly means is 6.20 ± 0.04 J/kg, while the maximum and minimum monthly means are 9.23 ± 0.05 J/kg in July 2015 and 4.75 ± 0.03 J/kg July 2013, respectively. Thus, the interannual variation from the maximum to the minimum is ~72.3%, which is computed as (maximum − minimum)/mean of 18 monthly means. The mean $E_{\rm pm}$ of the three winters (2012, 2015, and 2018) with a QBO easterly phase is 8.12 ± 0.03 J/kg, while the mean of the rest six winters in the QBO westerly phase is 5.23 ± 0.05 J/kg. Hence, the $E_{\rm pm}$ winter maxima are ~43% higher in the easterly phase than in the westerly phase of the QBO (the definition of QBO phases will be given in section 4). To inspect whether the interannual variations of N^2 are sufficient to account for the observed $E_{\rm pm}$ variations, the harmonic fittings given by Equation 4 are applied to nine individual years of the buoyancy frequency square N^2 in Figure 2a and to all years in Figure 2b. The fitting parameters and their errors are listed in Table 6, and the fitted results are plotted as red curves in Figure 2. The interannual variations of N^2 winter maxima are less than 7%, which is insufficient to explain the $E_{\rm pm}$ interannual variations.

We now derive the mean annual cycle in $E_{\rm pm}$, $E_{\rm pv}$, and N^2 in order to account for and subtract the annual cycle to isolate QBO signatures in section 4. Figure 3 shows 9 years of data binned every 5 days to form composite annual data sets of $E_{\rm pm}$, $E_{\rm pv}$, and N^2, respectively. Harmonic fittings of the annual plus semiannual oscillations given by Equation 4 are applied to the composite years for all three parameters. The fitting parameters and their errors are listed in Tables 4, 5, and 6 for $E_{\rm pm}$, $E_{\rm pv}$, and N^2, respectively, while the fitted results are shown as red curves in Figure 3. The 9-year results are consistent with the $E_{\rm pm}$ and N^2 composite annual variations derived from 5 years of data (2011–2015) shown in Chu et al. (2018). Winter maxima occurring at the beginning of July are evident in all three parameters.

4. QBOs in Antarctic Gravity Wave $E_{\rm pm}$ and Polar Vortex Location

The QBO was originally discovered as the alternation between the downward propagating easterly and westerly zonal wind regimes in the equatorial stratosphere (~16–50 km) with variable periods from 22 to

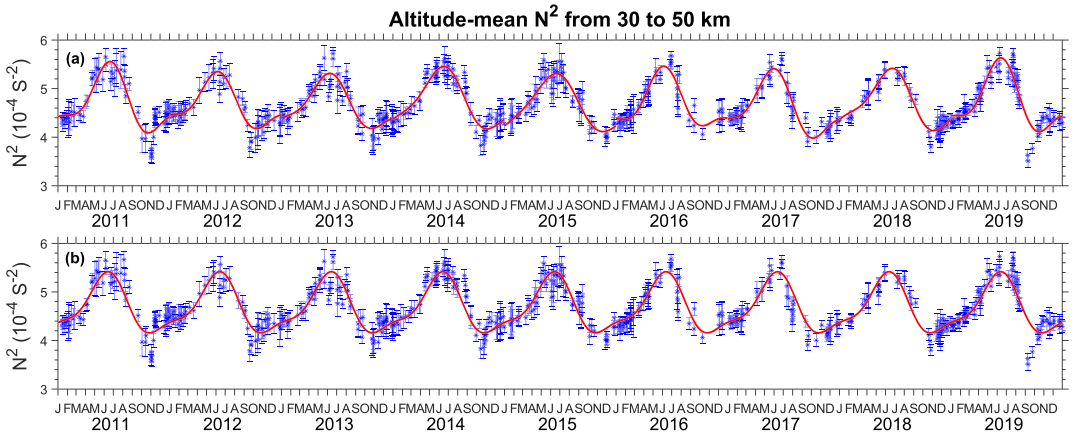

Figure 2. Altitude mean N^2 from 30 to 50 km through 9 years, 2011–2019. Each blue asterisk denotes a single observational segment with error bar. The red lines are (a) single-year "annual + semiannual" fits for nine individual years, and (b) uniform "annual + semiannual" fits for all years.

34 months (see a review by Baldwin et al., 2001). Singapore radiosondes have been used to characterize the QBO index since 1980, and the zonal-mean zonal winds of MERRA-2 at the equator give nearly identical results as the Singapore sondes (https://acd-ext.gsfc.nasa.gov/Data_services/met/qbo/qbo.html). We abbreviate the QBO easterly phase as QBOe and the QBO westerly phase as QBOw. Due to the downward progression of the zonal wind regimes, QBO indices defined at different pressure levels can alter the classification of QBOe and QBOw for some years, and consequently different studies use different QBO indices (e.g., Anstey & Shepherd, 2014; Baldwin & Dunkerton, 1998; Hitchman & Huesmann, 2009; Lu et al., 2019). Comparing three QBO indices in section 4.2 (Figure 5), we find that there are stable years whose QBO phase classifications remain the same, while there are also transition years whose QBO phases strongly depend on the pressure levels used for the QBO indices. It is worth pointing out that 2016 is abnormal among the last 40 years (1980–2019). Year 2016 went through a brief period of QBO easterly phase when a QBO index at 40–50 hPa is used (see Figures 4a and 5c) but stayed in the QBO westerly phase when a QBO index at 20–30 hPa is used (see Figure 5b). Newman et al. (2016) studied this anomalous change in the QBO in the northern winter 2015–2016 and pointed out that easterlies unexpectedly appeared in the westerly phase of the QBO. This abnormality is kept in mind during our studies below.

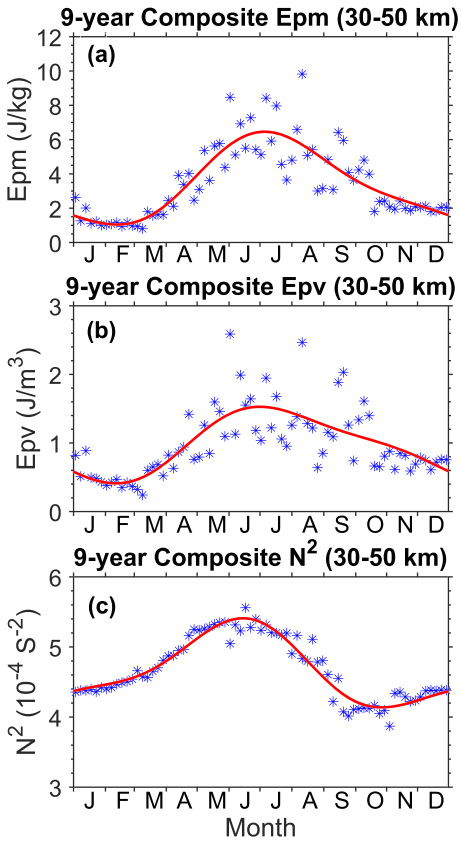

Figure 3. Nine-year composite-mean annual cycles of (a) E_{pm}, (b) E_{pv}, and (c) N^2. Data are binned every 5 days at McMurdo. The red lines are the harmonic fits given by Equation 4.

4.1. QBO Signals in the E_{pm} Anomaly of Antarctic Gravity Waves

We investigate the observed interannual variations of winter E_{pm} for possible signatures of the QBO. A QBO index, defined as the MERRA-2 zonal-mean zonal winds at the equator (0° latitude) averaged over the 40 and 50 hPa pressure levels, is plotted versus the 9 years of lidar-observed E_{pm} data and harmonic fittings in Figure 4a. According to this QBO index, 2012, 2015, and 2018 midwinters are classified as QBOe, while 2011, 2013, 2014, 2017, and 2019 are classified as QBOw. The year 2016 is abnormal as stated above—although the QBO index at 40–50 hPa is negative, the majority of pressure levels classify the 2016 southern winter into the westerly phase (positive index). The Antarctic winters of 2012 and 2015 both occur in the QBO easterly phase and correspond to high E_{pm} peaks. Although the winter

Table 5
Harmonic Fitting Parameters and Errors for $\overline{E}_{pv}$ in Figures 1 and 3

Case	A_0 ($\times 10^{-2}$ J/m^3)	A_{12} ($\times 10^{-2}$ J/m^3)	φ_{12} (day)	A_6 ($\times 10^{-2}$ J/m^3)	φ_6 (day)
Figure 1c (2011)	1.19 ± 0.10	0.44 ± 0.14	234 ± 17	0.45 ± 0.13	93 ± 9
Figure 1c (2012)	1.21 ± 0.10	0.66 ± 0.14	195 ± 14	0.49 ± 0.14	163 ± 9
Figure 1c (2013)	0.97 ± 0.07	0.25 ± 0.09	184 ± 25	0.15 ± 0.10	136 ± 20
Figure 1c (2014)	0.95 ± 0.07	0.41 ± 0.11	230 ± 13	0.02 ± 0.10	116 ± 132
Figure 1c (2015)	1.20 ± 0.11	0.96 ± 0.15	194 ± 10	0.16 ± 0.15	178 ± 30
Figure 1c (2016)	1.07 ± 0.08	0.51 ± 0.12	256 ± 12	0.29 ± 0.10	140 ± 10
Figure 1c (2017)	0.82 ± 0.07	0.45 ± 0.08	193 ± 15	0.22 ± 0.11	162 ± 12
Figure 1c (2018)	0.87 ± 0.07	0.47 ± 0.01	211 ± 11	0.30 ± 0.09	209 ± 10
Figure 1c (2019)	0.76 ± 0.07	0.40 ± 0.09	206 ± 16	0.09 ± 0.09	203 ± 37
Figure 1d (uniform)	0.99 ± 0.03	0.49 ± 0.04	207 ± 5	0.11 ± 0.04	154 ± 10
Figure 3b (composite)	0.99 ± 0.04	0.51 ± 0.06	206 ± 7	0.12 ± 0.06	154 ± 14

maximum in 2018 is not as high as the maxima in 2012 and 2015, likely due to the lack of lidar data in June 2018, it is still larger than the surrounding years like 2016, 2017, and 2019. The overall mean E_{pm} in June and July over three QBOe years (2012, 2015, and 2018) are ~43% higher than the overall mean during the QBOw years (the other six years), as computed in section 3. This E_{pm} interannual variation has a period of roughly 3 years, rather than the 28 month quasi-biennial period (Baldwin et al., 2001). A wavelet analysis of the QBO index at 25 hPa in Lu et al. (2019) shows that the QBO period has evolved from ~24 to ~36 months between 2003 and 2018, which is consistent with the longer QBO period in the last decade of lidar observations.

To quantify the correlation between the gravity wave E_{pm} and QBO index, we compute the E_{pm} anomaly, wherein seasonal variations are removed. We use the harmonic fittings of nine individual years to represent the yearly E_{pm} values and the composite-mean fit in Figure 3a as the mean annual cycle of E_{pm} and then subtract the mean annual cycle from the nine individual harmonic fittings to derive the E_{pm} anomalies. The derived E_{pm} anomalies of two winter months (June and July) are plotted as diamonds in Figure 4a, except for 2016 and June 2018 that are plotted as squares. These results show that the positive/negative anomalies align well with the negative/positive QBO index (easterly/westerly zonal winds at the equator), except during the abnormal year 2016. All positive E_{pm} anomalies occur in the three QBO easterly years (2012, 2015, and 2018). In Figure 4b we plot the monthly mean E_{pm} anomalies versus the monthly mean QBO index for June and July. Because 2016 is an abnormal year and 2018 lacks June data, Figure 4b excludes 2016 data and 2018 June data. Based on the remaining 15 data points, the linear correlation coefficient between the E_{pm} anomaly and the QBO index at 40–50 hPa is −0.766 with a confidence level of 99.9%. This statistically significant correlation between the gravity wave E_{pm} and QBO phase supports that the stratospheric gravity wave activity is stronger in the QBO easterly winters than in the westerly winters, at least during the last decade. The observed interannual variations of E_{pm} are likely due to the modulation by the QBO signals.

Table 6
Harmonic Fitting Parameters and Errors for N^2 in Figures 2 and 3

Case	A_0 ($\times 10^{-4}$ s^{-2})	A_{12} ($\times 10^{-4}$ s^{-2})	φ_{12} (day)	A_6 ($\times 10^{-4}$ s^{-2})	φ_6 (day)
Figure 2a (2011)	4.70 ± 0.03	0.61 ± 0.03	157 ± 4	0.27 ± 0.04	179 ± 4
Figure 2a (2012)	4.67 ± 0.02	0.49 ± 0.03	145 ± 4	0.21 ± 0.03	167 ± 4
Figure 2a (2013)	4.67 ± 0.02	0.51 ± 0.03	148 ± 4	0.16 ± 0.03	171 ± 6
Figure 2a (2014)	4.75 ± 0.02	0.60 ± 0.02	155 ± 3	0.14 ± 0.03	183 ± 5
Figure 2a (2015)	4.67 ± 0.02	0.57 ± 0.03	161 ± 3	0.09 ± 0.03	191 ± 9
Figure 2a (2016)	4.69 ± 0.02	0.54 ± 0.03	153 ± 3	0.24 ± 0.03	161 ± 3
Figure 2a (2017)	4.60 ± 0.02	0.61 ± 0.03	137 ± 2	0.24 ± 0.03	164 ± 3
Figure 2a (2018)	4.72 ± 0.01	0.57 ± 0.02	160 ± 2	0.17 ± 0.02	190 ± 3
Figure 2a (2019)	4.73 ± 0.01	0.64 ± 0.03	154 ± 3	0.28 ± 0.04	173 ± 3
Figure 2b (uniform)	4.69 ± 0.01	0.57 ± 0.01	154 ± 1	0.18 ± 0.01	175 ± 2
Figure 3c (composite)	4.69 ± 0.01	0.57 ± 0.02	152 ± 2	0.18 ± 0.02	176 ± 3

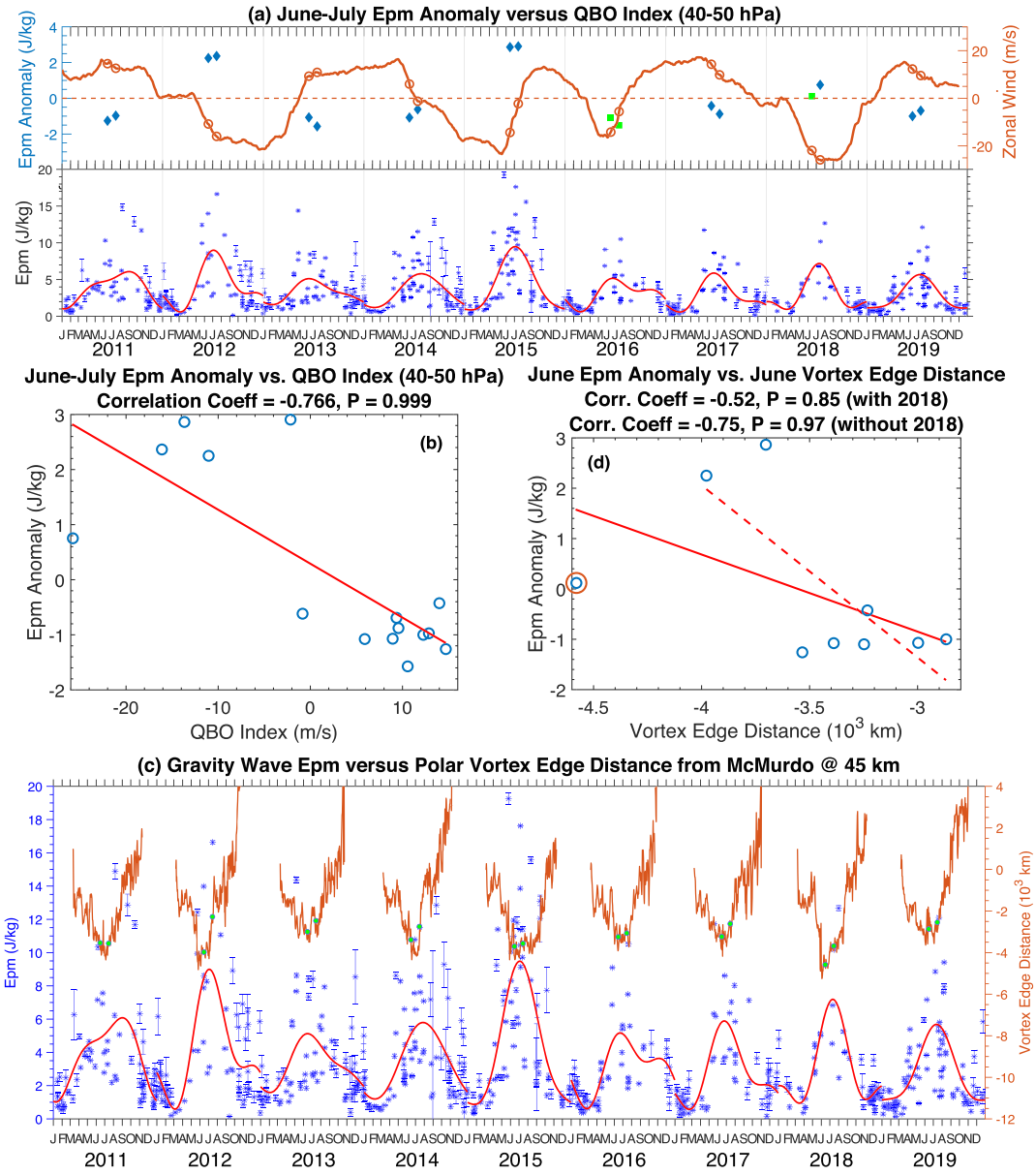

Figure 4. (a) The equatorial zonal-mean zonal winds averaged over 40 and 50 hPa are plotted as the QBO index (orange curve) for 9 years from 2011 to 2019. Orange circles mark the QBO index at 15 June and 15 July. The QBO data are taken from MERRA-2 at daily resolution with seven-point running smooth. Monthly mean E_{pm} anomalies for June and July are plotted as blue diamonds for the 9-year lidar observations except June and July 2016 and June 2018 that are plotted in green squares. The lidar-observed E_{pm} data points with harmonic fittings (as Figure 1a) are shown in the bottom portion against the QBO index at the top for comparison. (b) Correlation between the monthly mean E_{pm} anomalies in June and July and the monthly mean QBO index at 40–50 hPa in June and July. The red line is a linear fit to the data points. The linear correlation coefficient is −0.766 at a confidence level (P) of 99.9%. (c) A 9-year time series of polar vortex edge distance from McMurdo at 45 km is plotted in the top portion against the 9 years of lidar-observed E_{pm} and harmonic fittings in the bottom portion. (d) The monthly mean E_{pm} anomalies in June versus the monthly mean vortex edge distance from McMurdo at 45 km altitude in June. The solid red line is a linear fit to all nine data points from 2011 to 2019, and the dashed red line is a linear fit to the data points excluding 2018 (circled with red color).

4.2. QBO Signals in the Antarctic Polar Vortex

We now investigate whether the E_{pm} enhancement in the QBO easterly winters is related to the polar vortex changes and whether the Antarctic polar vortex is also affected by the equatorial QBO signals. This work is motivated by the findings shown in Figure 10 of Chu et al. (2018), namely, that the maximum E_{pm} values occur in June and July when McMurdo is deep inside the polar vortex. At the time of publication of Chu et al. (2018) the correlation of E_{pm} with McMurdo distance from the vortex edge was disputed as a

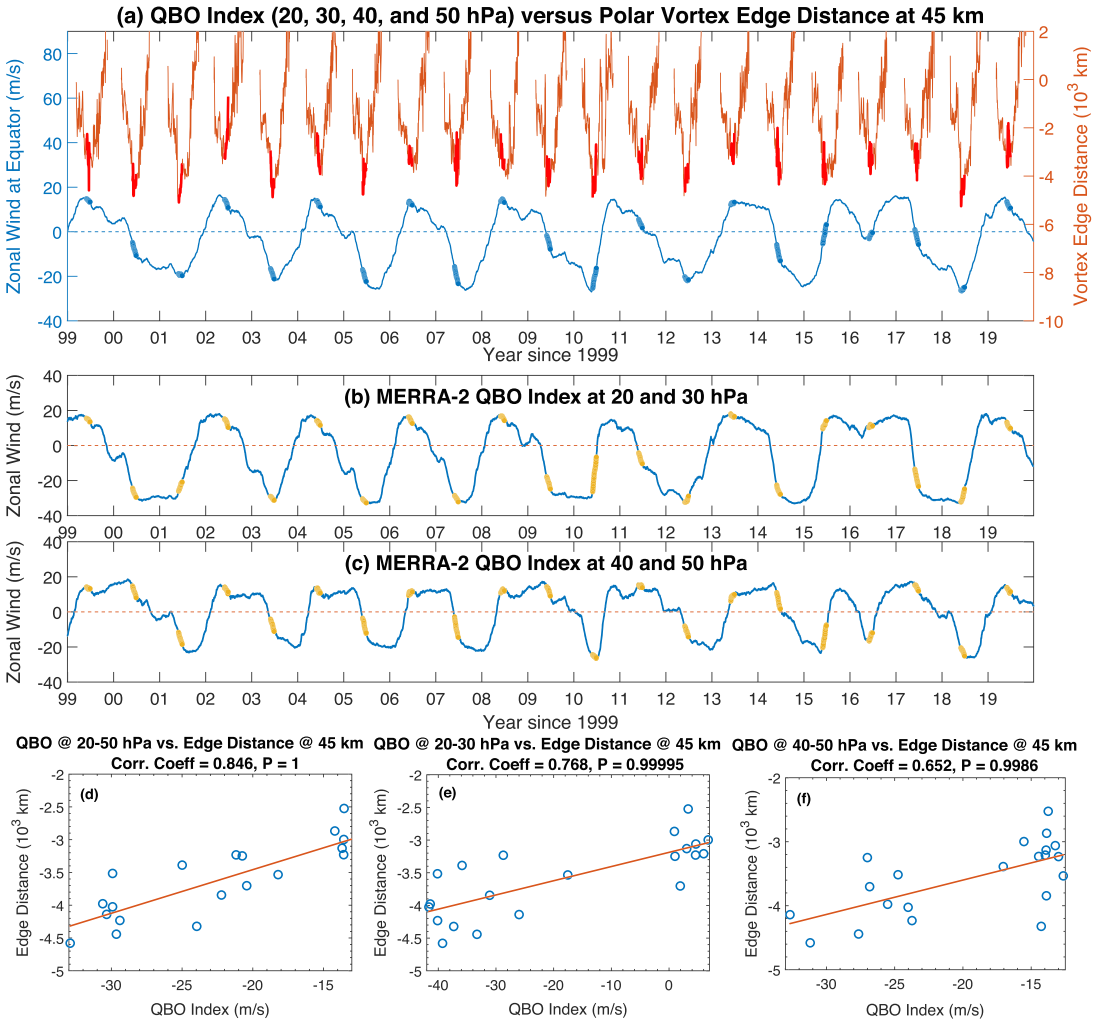

Figure 5. (a) A 21-year time series (1999–2019) of the distance between McMurdo and the polar vortex edge at 45 km altitude (reddish-brown curves). Negative/positive distance denotes that McMurdo is inside/outside the polar vortex. The blue curves are the vertically integrated QBO index that is derived from the zonal-mean zonal wind at the equator averaged over pressure levels of 20, 30, 40, and 50 hPa. The red dots on the reddish-brown vortex edge distance curves and the blue dots on the blue QBO index curves mark the 30 days in June for each of the 21 years. (b) QBO index derived from the zonal-mean zonal wind at the equator averaged over pressure levels of 20 and 30 hPa. Gold dots mark the 30 days in June for each year. (c) QBO index derived from the zonal-mean zonal wind at the equator averaged over pressure levels of 40 and 50 hPa. Gold dots mark the 30 days in June for each year. (d, e, f) Correlations of the mean vortex edge distance in June at 45 km with three different QBO indices in June that are shown in panels (a)–(c), respectively. The linear correlation coefficients in the three cases are 0.846, 0.768, and 0.652 with confidence levels (P) above 99%.

coincidence with the peak of E_{pm} seasonal variations. Now in light of evidence of the QBO in the interannual variations of E_{pm}, it may not be a coincidence anymore. The shortest distance from McMurdo to the polar vortex edge is calculated on each day using the MERRA-2 reanalysis data as described in section 2.3 and is termed "vortex edge distance." Negative/positive vortex edge distances mean that McMurdo is inside/outside the polar vortex. Vortex edge distances are negative during the Antarctic winter due to McMurdo being located deep inside the core of the vortex. The 9-year time series of vortex edge distance at 45 km is plotted against the time series of E_{pm} in Figure 4c. Visual inspection of these two time series suggests that winters with lower E_{pm} maxima, such as in 2013 and 2016, correspond to the shorter vortex distances, that is, less negative values that occur when the vortex edge is closer to the McMurdo Station, while winters with high E_{pm} maxima, such as in 2012, 2015 and 2018, correspond to the longer (more negative) vortex edge distances when the vortex edge is farther away from McMurdo Station. Figure 4d shows the mean E_{pm} anomaly in June versus the mean vortex edge distance in June. A linear fit gives a correlation coefficient of −0.52 with a confidence level of 85% when all 9 years of lidar data are included.

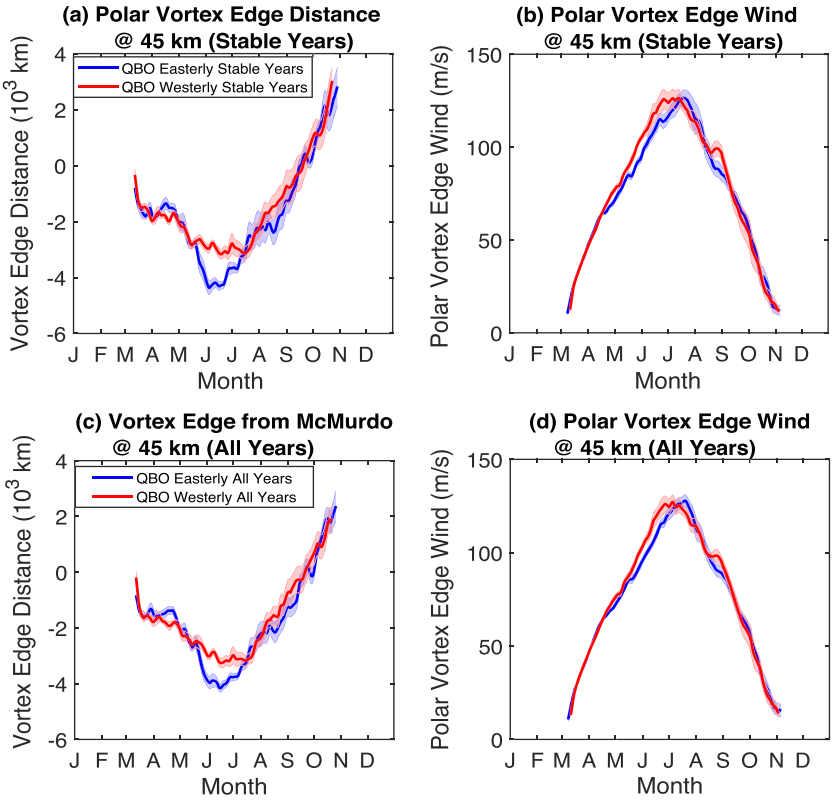

Figure 6. (a) The mean vortex edge distance averaged over stable QBO easterly years (2001, 2003, 2005, 2007, 2010, 2012, and 2018) is compared with that averaged over stable QBO westerly years (1999, 2002, 2004, 2006, 2008, 2013, and 2019). The QBOe and QBOw results are plotted in blue and red colors, respectively. The over-plotted shades represent the standard deviation, that is, the distribution, of vortex edge distance. (b) Mean wind speeds averaged along the polar vortex edge for the stable easterly and westerly years, respectively. The standard deviations are over-plotted on the edge wind speed curves. (c and d) The same as (a) and (b), except for all years of QBOe (2000, 2001, 2003, 2005, 2007, 2009, 2010, 2012, 2014, 2015, 2017, and 2018), and all years of QBOw (1999, 2002, 2004, 2006, 2008, 2011, 2013, 2016, and 2019). A seven-point running smooth with one-point step is applied to all curves shown in (a)–(d).

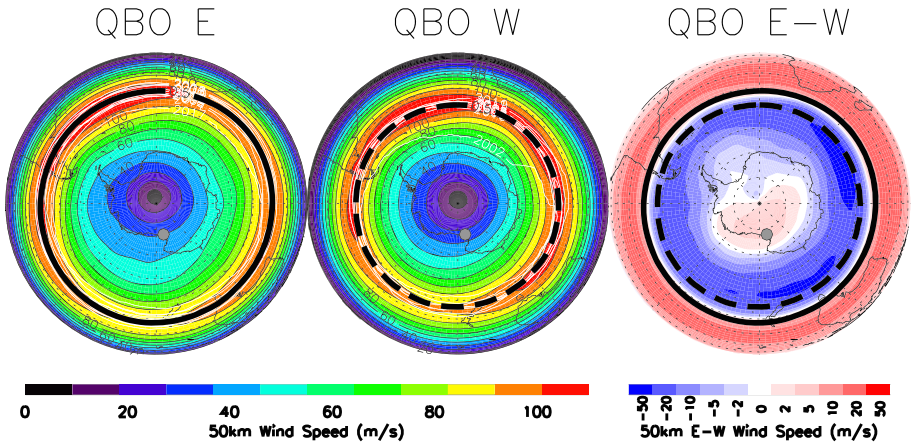

Figure 7. Southern Hemisphere polar maps of the June average wind speed (color fill) at 50 km altitude for all QBO easterly years (left), westerly years (middle), and the difference (right). The June mean vortex edge is shown using a thick solid (dashed) black contour for QBOe (QBOw) years. Monthly mean June vortex edge locations for individual years are the thin white contours in the left and middle panels. McMurdo Station is indicated by the gray filled circle.

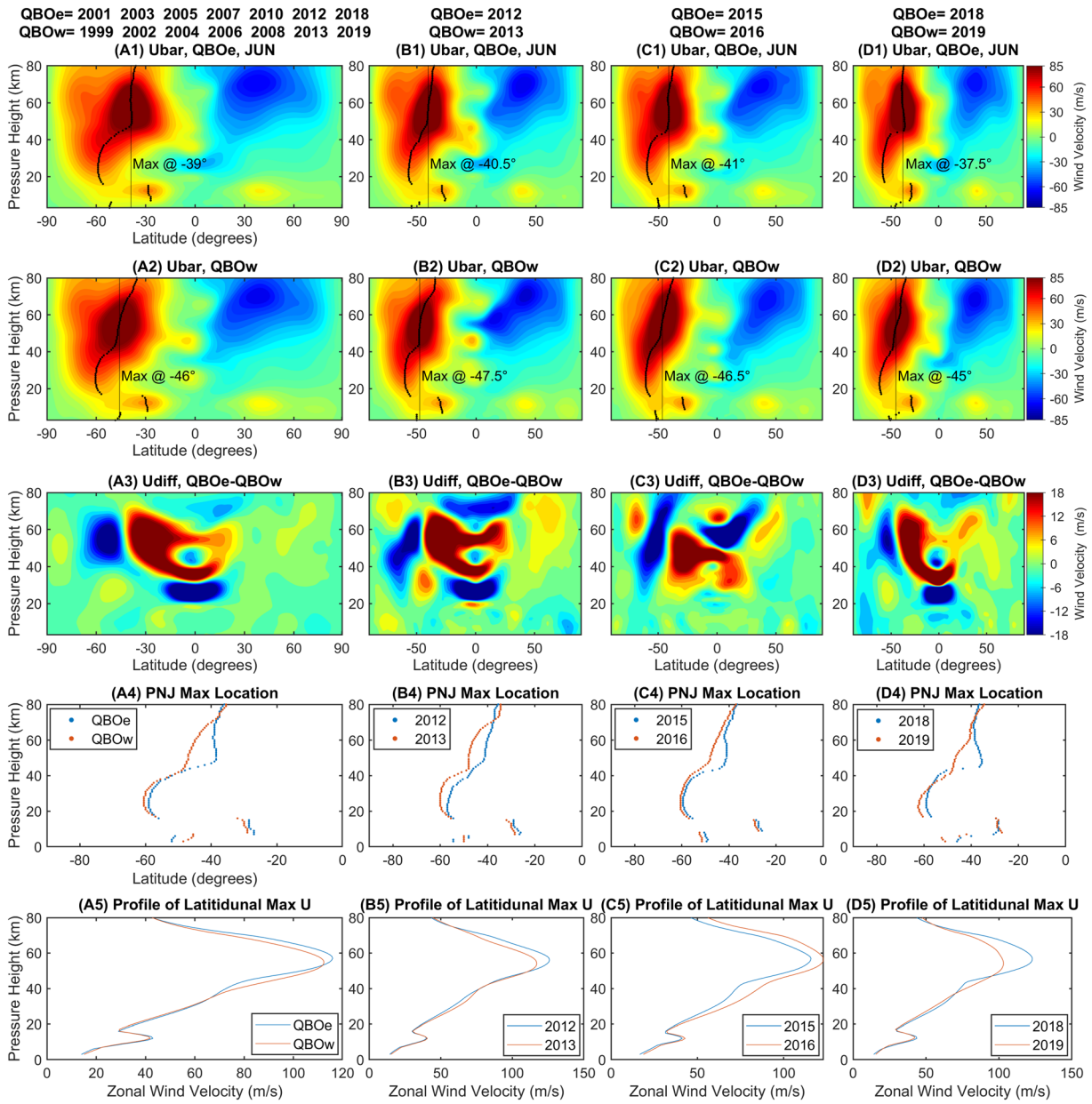

Figure 8. (first row) Mean June zonal-mean zonal winds for stable QBO easterly winters (left) and zonal-mean zonal winds in 2012, 2015, and 2018 (QBO easterly June). (second row) Mean June zonal-mean zonal winds in the stable QBO westerly winters (left), and zonal-mean zonal winds in 2013, 2016, and 2019 (QBO westerly June). (third row) Easterly anomaly of zonal-mean zonal winds (QBOe − QBOw) in June, that is, first row minus second row. (fourth row) Latitude of the June maximum wind velocity during QBOe (blue) and QBOw (red). (fifth row) Magnitude of the June maximum zonal wind velocity during QBOe (blue) and QBOw (red).

If June 2018 data is excluded because of the lack of lidar observations in that month, then the correlation coefficient becomes −0.75 with a confidence level of 96.7%. Figure 4d indicates that with or without June 2018 data the negative correlation between E_{pm} anomalies and polar vortex edge distances is clear. The June 2018 fitting data is likely an outlier, which was very likely biased toward smaller values due to the lack of observational data at a time when E_{pm} is usually the highest. While a longer data record is needed, Figures 4c and 4d indicate a possible QBO signal in the polar vortex edge location and a correlation between the E_{pm} anomaly and the vortex edge distance.

To further investigate the QBO signals in the polar vortex location, we plot the time series of 21 years (1999–2019) of vortex edge distance at 45 km in the upper portion of Figure 5a. The vortex edge distance in

June (red color) is farther (more negative edge distances) in the QBOe (negative QBO winds) and closer (less negative edge distances) in the QBOw (positive QBO winds). Three different QBO indices are shown in the bottom portion of Figures 5a–5c. The new QBO index in Figure 5a is defined as the zonal-mean zonal wind at the equator averaged over pressure levels of 20, 30, 40, and 50 hPa, while the QBO indices in Figures 5b and 5c are the zonal winds averaged over pressure levels of 20 and 30 hPa and over pressure levels of 40 and 50 hPa, respectively. As mentioned earlier, different QBO indices defined at different pressure levels can alter the QBO easterly and westerly classifications for some June months. For example, 2000, 2009, 2011, 2014, 2015, 2016, and 2017 flip signs between the 20–30 hPa QBO index of Figure 5b and the 40–50 hPa QBO index of Figure 5c. At the same time, 2001, 2003, 2005, 2007, 2010, 2012, and 2018 remain in the QBO easterly phase, while 1999, 2002, 2004, 2006, 2008, 2013, and 2019 remain in the QBO westerly phase under all three QBO indices. The monthly means of vortex edge distance in June at 45 km altitude are plotted against the June means of three different QBO indices in Figures 5d–5f, respectively. All three figures show positive correlations between the vortex edge distance and the QBO indices, that is, more negative vortex edge distances (McMurdo is inside and farther from the vortex edge) correspond to more negative (easterly) QBO winds. Likewise, less negative vortex edge distances (McMurdo is inside but closer to the vortex edge) correspond to more positive (westerly) QBO winds. The linear correlation coefficients are 0.846, 0.768, and 0.652 with confidence levels of 100%, 99.995%, and 99.863%, respectively. Over this 21-year period, the QBO signals in the polar vortex edge location are robust and have statistical significance. The new QBO index given in Figure 5a has the highest correlation with the vortex edge distance. This new index is the integration (i.e., the mean) of all four pressure levels of 20, 30, 40, and 50 hPa, reflecting the downward progression of the equatorial zonal wind better than other two indices. This analysis convincingly shows that the polar vortex edge moves equatorward in the QBO easterly winters and moves poleward in the QBO westerly winters.

Winters (June) with consistent easterly (2001, 2003, 2005, 2007, 2010, 2012, and 2018) or westerly (1999, 2002, 2004, 2006, 2008, 2013, and 2019) classifications (they do not flip signs for different QBO indices) are termed the "stable years" (stable winters) of QBOe or QBOw, while the rest (2000, 2009, 2011, 2014, 2015, 2016, and 2017) are called "transition years." The set including both stable and transition years is referred to as the "all years" set. Using the vertically integrated QBO index given in Figure 5a, we classify the "all years" set of QBO easterly winters as (2000, 2001, 2003, 2005, 2007, 2009, 2010, 2012, 2014, 2015, 2017, and 2018) and the "all years" set of QBO westerly winters as (1999, 2002, 2004, 2006, 2008, 2011, 2013, 2016, and 2019). We now average the vortex edge distance and mean wind speed along the vortex edge within these two groups. Two trials are made—one averages over the stable years of QBOe and QBOw, and another averages over the "all years" sets for QBOe and QBOw. The "stable years" results are compared in Figures 6a and 6b, and the "all years" results are in Figures 6c and 6d for the vortex edge at 45 km altitude. It is clear in both cases that the polar vortex edge stays farther away from McMurdo in the QBO easterly years than in the westerly years during the midwinter, and the differences in vortex edge distance reach the maximum in June with a time span of about 2 months (from mid-May to mid-July). The differences in the means of the stable winters (about 1,200 km) are larger than those in the means of "all years" winters (about 900 km), as expected. The differences in the mean winds along the vortex edge are relatively small, but in general the mean winds in the QBOe are weaker than in the QBOw by about 10–20 m/s in June. Note that the QBO differences seen in vortex edge distance and vortex edge wind speed are seasonally dependent.

To further investigate the polar vortex changes, three panels of polar vortex maps in the Southern Hemisphere (SH) are plotted in Figure 7. All panels are derived from MERRA-2 reanalysis data from 1999 to 2019 for June near 50 km altitude. The left panel shows the average June wind speed (in color) and Antarctic vortex edge (thick black contour) for QBO easterly years. The thin white contours are the vortex edge for the individual easterly years. The middle panel is the June average for QBO westerly years. The right panel is the difference (QBOe − QBOw) in wind speed (blue/red colors) and the mean vortex edge for easterly years (solid black) and for westerly years (dashed black). This right panel shows that the zonal wind over McMurdo (marked by a gray filled circle) is ~5–10 m/s faster in the QBOe than in the QBOw at 50 km. The blue shades from 40–70°S latitudes and the red shades equatorward of 40°S in the right panel of Figure 7 reflect an equatorward shift in the PNJ during QBO easterly years. In terms of the vortex edge, the June mean vortex edge is located at 39.7°S latitude during QBO easterly years and at 47.7°S latitude during QBO westerly years (right panel) when all years of QBOe and QBOw are included. Removing two sudden stratospheric warming (SSW) years (2002 and 2019) from QBOw, the mean vortex edge in June is located

at 39.7°S and 47.2°S for QBOe and QBOw, respectively, making only a 6% difference. The difference of 7.5–8°S latitude between the QBOe and QBOw years is statistically significant and it confirms that the QBO signals in the vortex edge distance shown in Figures 5 and 6 are robust.

5. Interannual Variations of PNJ in June and Critical Level Filtering Effects

5.1. Equatorward Shift of the SH PNJ in June During QBOe

Our results indicate that the QBO signals in the Antarctic polar vortex edge location are largest in June. This finding prompts us to examine the PNJ in June in order to understand the environment surrounding the polar vortex. We average the MERRA-2 zonal-mean zonal winds (U-bar) over the stable years of QBOe and QBOw, respectively, for June in Figures 8a1 and 8a2, and take the differences between them in Figure 8a3. This differentiation method is similar to that of Baldwin and Dunkerton (1998), Hitchman and Huesmann (2009), and Lu et al. (2019). As MERRA-2 is a pressure level-based model, the data are converted to pressure heights (z) using the equation $z = H \cdot \log(p_o/p)$, where the scale height (H) is set to 7 km and $p_o = 1{,}000$ hPa. On these plots, the PNJ core is defined as the maximum zonal wind velocity (eastward) in the latitude-altitude plane and is overlaid for each altitude on Figures 8a1 and 8a2, as well as its location reiterated and value displayed in Figures 8a4 and 8a5, respectively.

From the Figures 8a1 and 8a2, we can see that the maximum U-bar occurs around 50 km altitude at −39° and −46° latitude for the QBOe and QBOw, respectively, showing that the PNJ core location moves equatorward in a QBO easterly phase as compared to a QBO westerly phase by ~7° latitude. Figure 8a3 displays the different responses of different regions to the changing QBO phase. Figure 8a4 shows that the maximum wind location varies with altitude, reaching equatorwardmost near the stratopause and lower mesosphere (~45–60 km) and slowly moving poleward with decreasing altitude to around −60° latitude in the lower stratosphere (~20–30 km). The equatorward shift during QBOe can again be seen here, but no major differences can be discerned in zonal wind velocity for any altitude between QBO phases in Figure 8a5. The shift in PNJ location seen in Figures 8a1–8a4 is a clear reflection of the vortex expansion during QBOe demonstrated above. During the QBO easterly phase, the polar vortex expands, pushing the PNJ toward the equator. It is worth mentioning that Yamashita et al. (2018) reported a seemingly opposite result in July that the QBO westerly phase corresponds to an equatorward vortex shift. However, further examination shows that a QBO index defined at 10–20 hPa in Yamashita et al. (2018) is almost opposite to the QBO phase classifications shown in our Figure 5a. Therefore, their results are basically consistent with our findings in June.

The easterly anomalies (QBOe − QBOw) in Figure 8a3 show a triple-cell structure from the equator to the South Pole around the stratopause. The June zonal-mean zonal winds in the QBOe are stronger in the equatorial to subtropical region (0–40°S), weaker in the midlatitude to high-latitude region (45–70°S), and slightly stronger in the polar region (75–90°S) than those in the QBOw between 40 and 70 km altitude. Such pattern around the stratopause is similar to the dipole-cell structure poleward of 30°S in August reported by Lu et al. (2019). This pattern also supports a finding of the northern-southern hemispheric asymmetry in the QBO easterly anomalies of zonal-mean zonal winds in Lu et al. (2019). The Northern Hemisphere QBO easterly anomalies in Figure 2 (D3) of Lu et al. (2019) reveal a two-cell structure from the equator to the North Pole around the stratopause in January, in contrast to the triple-cell structure shown here. Our tests have revealed that this triple-cell pattern around the stratopause is robust in June, insensitive to including or removing years from the data set. Figure 8a3 shows negligible differences between QBOe and QBOw below 30 km in the polar region in June, which agrees with the August result of Baldwin and Dunkerton (1998). Columns 2–4 of Figure 8 are included to demonstrate that variability exists between years, but the QBO phase-related behavior is still well represented by the "stable" years used in Column 1. The three displayed QBO easterly winters (2012, 2015, and 2018) have higher June and July E_{pm} values than other years and correspond to the equatorward shifted PNJ as compared to the adjacent QBO westerly winters (2013, 2016, and 2019). It can also be seen that the trends demonstrated in each row of plots are similar from column to column.

5.2. Effects of Critical Level Filtering on Gravity Wave E_{pm}

Why does an equatorward expanding vortex (in QBOe) correspond to enhanced E_{pm}? There may be several factors contributing to this correlation with critical level filtering as one of the major factors. The expanding

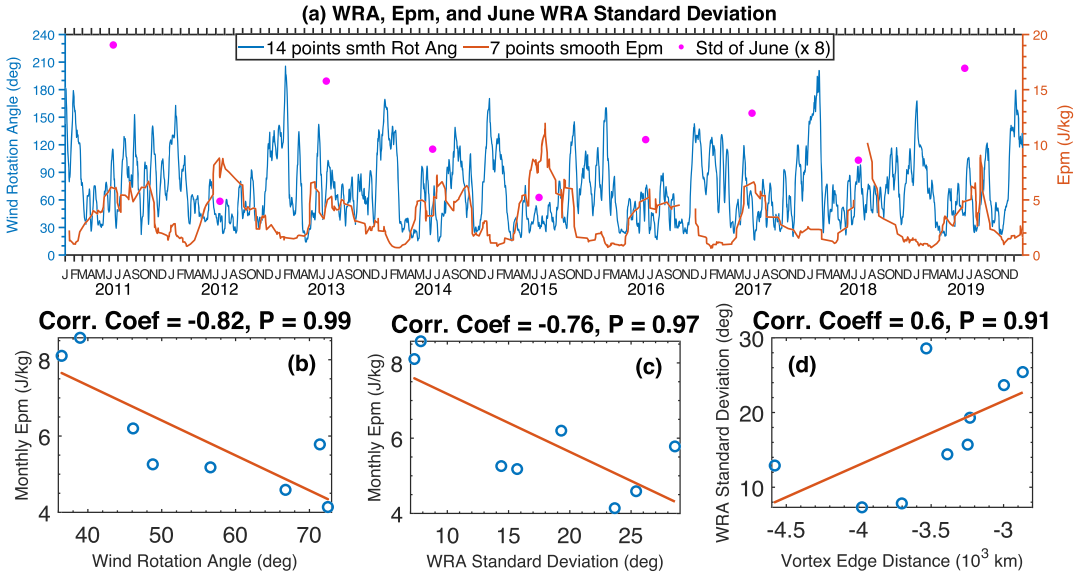

Figure 9. (a) Time series of wind rotation angle between 11 and 30 km versus the gravity wave E_{pm}. A 14- day running smooth with one- day step is applied to the WRA (blue curve). A seven-point running smooth at one-point step is applied to the lidar-measured E_{pm} (red curve); data gaps in November 2016 and June 2018 are due to the lack of qualified data. The magenta circles are the standard deviations of WRA in June multiplied by a factor of 8 for clarity. (b) Correlation between monthly mean E_{pm} in June and monthly mean WRA in June from 2011 to 2019. The data are taken from the red and blue curves in (a). (c) Correlation between June mean E_{pm} and WRA standard deviation from 2011 to 2019. (d) Correlation between mean June vortex edge distance from McMurdo and WRA standard deviation from 2011 to 2019.

vortex likely corresponds to a quieter polar region characterized by horizontal wind profiles being less variable with altitude. Quieter winters likely have less critical level filtering, thereby higher probability for gravity waves to reach the upper stratosphere. To evaluate this hypothesis, we investigate the interannual variations of WRA and the potential correlation to those of E_{pm}. WRA is a measure of the critical level filtering as discussed in Chu et al. (2018) and Yamashita et al. (2009). Following the denotation in Chu et al. (2018) we compute WRA near McMurdo as the maximum wind direction change from 11 to 30 km. Nine MERRA-2 grid points near McMurdo within the spatial box of 77–78°S latitude by 166.25–167.5°E longitude are used in this computation. We first average the horizontal winds within the nine grid points for each altitude then trace the wind direction changes from the lowest to the highest altitudes under the assumption that the wind direction changes between two adjacent altitude bins (~1 km interval) do not exceed 180° and finally calculate the angle between the two outmost flanks of wind directions as the WRA. Figure 8b3 shows that the upper stratosphere and lower mesosphere zonal winds are weaker in QBOe (2012) than in QBOw (2013) from 60°S to 80°S, while the lower stratospheric and tropospheric zonal winds are stronger in QBOe than in QBOw, as can be seen from the positive cell around 75°S at 7 km. As a result, the WRA calculated from MERRA-2 data is smaller and less variable in 2012 than in 2013 (see Figure 9a). Smaller and less variable WRAs in midwinter 2012 indicate less critical level filtering, thereby a higher probability for gravity waves to reach 30–50 km, leading to higher E_{pm} in 2012 than in 2013.

To investigate this relation further, the seven-point running smoothed gravity wave E_{pm} is plotted in Figure 9a (red curves) to compare with the WRA (blue curves). The gaps in Nov 2016 and June 2018 are due to the lack of qualified lidar data. The anticorrelation between the E_{pm} and WRA is considered to be the main cause of the summer-winter asymmetry in the seasonal variations of E_{pm} as studied in Chu et al. (2018). What we care about here is whether the interannual variations of WRA can account for the interannual variations of E_{pm} in the midwinter. For this purpose, we take the June means of the E_{pm} and WRA curves in Figure 9a, respectively, and plot their correlation in Figure 9b. The standard deviation of the WRA in June is plotted against the June mean E_{pm} in Figure 9c. Negative correlations of −0.82 and −0.76 are obtained with the confidence levels of 99% and 97% in Figures 9b and 9c, respectively. The

standard deviation of WRA is used here to represent the stability of the background winds, which may be affected by the relative location between McMurdo and the vortex edge. When the polar vortex edge moves equatorward, thus McMurdo being well inside the polar vortex, the background winds are likely more stable, thereby lower standard deviation of WRA and less critical level filtering are expected. Plotting the WRA standard deviation in June against the vortex edge distance in June in Figure 9d, we do see a positive correlation of ~0.6, although the confidence level (91%) is less than 95%. The results above support the hypothesis that the interannual variations of E_{pm} is mainly determined by the interannual variations of WRA that is strongly influenced by the polar vortex location in the midwinter. The equatorward expansion of the polar vortex in the QBO easterly phase leads to quieter winters and more stable background winds that correspond to less critical level filtering and thus higher E_{pm} in the upper stratosphere. Lidar observations in Alaska also show significant interannual variations in gravity wave E_{pm} averaged over three winter months (December, January, and February) from 40 to 50 km (Triplett et al., 2017). The highest gravity wave activity occurred during quiet winters when no SSW occurred, and the lowest gravity wave activity in the disturbed winters when major SSWs occurred (Triplett et al., 2017). These Arctic results are basically consistent with our findings of higher E_{pm} occurring in quieter Antarctic winters (QBOe).

6. Discussion

There are additional long-term variations that affect the polar wind and temperature fields, thus influencing the interannual variations of gravity waves and polar vortex. Here we briefly discuss two major factors—the solar cycle and the El Niño–Southern Oscillation (ENSO). The Holton-Tan effect, based on the Northern Hemisphere studies (Holton & Tan, 1988), emphasizes that the effective waveguide for upward and equatorward propagating planetary-scale waves is altered by the tropical winds. The zonal wind structure in the QBO easterly phase focuses more wave activity toward the pole, where planetary waves converge and slow down the zonal-mean flow. Hence, the Arctic polar winter vortex tends to be disturbed and weak when the QBO is easterly but undisturbed and strong when the QBO is westerly. Baldwin et al. (2001) point out that the QBO acts as predicted by Holton and Tan (1980) only in years with low solar activity but appears to reverse its behavior during years with high solar activity (Labitzke, 1987; Labitzke & van Loon, 1988; van Loon & Labitzke, 1994). Given the interhemispheric asymmetry in the QBO easterly anomalies (section 5.1), it is necessary to examine the response of QBO signals to solar activity in the SH. Analyzing the 21-year time series in Figure 5a, 1999–2003 corresponds to a solar maximum, while 2006–2011 corresponds to a solar minimum; however, the equatorward shift of the SH polar vortex in the QBOe occurs during both the solar maximum and minimum periods. To the first order, the robust QBO signals in the latitudes of vortex edge and PNJ are not affected by solar activity.

ENSO has been shown to affect the latitude of the June PNJ (Yamashita et al., 2018). The ENSO index used in that work was calculated from the 5 month running mean data of the Nino 3.4 index (NINO3.4) (http://www.esrl.noaa.gov/psd/data/correlation/nina34.data) provided by the National Oceanic and Atmospheric Administration (NOAA)/Earth System Research Laboratory. We find no correlation between the ENSO index and the vortex edge distance from 1999 to 2019 or from 1980 to 2019. Even after separating the vortex edge distance data into the QBOe and QBOw phases, there is still no statistically significant correlation. Therefore, the QBO signals in the vortex edge location and the latitude of the PNJ are robust and are not attributed to ENSO. Investigating the relationship between the ENSO index and the lidar-observed E_{pm}, we note a possible link between a particularly strong ENSO year and the year of our highest E_{pm} measurement (2015). However, there is no individual year correlation between ENSO and E_{pm} in the last decade. For example, 2019 corresponds to the second highest ENSO index among the nine years of 2011–2019 but one of the lowest E_{pm} winter maxima, while 2012 and 2018 correspond to the second and third highest E_{pm}, but the ENSO indices in these two years are lower than that in 2019. Therefore, it is most likely that the interannual variations of the gravity wave E_{pm} are mainly controlled by the QBO signals, not the ENSO effects, although the possible influence of ENSO on the highest E_{pm} year is noticeable and a longer data record is needed to draw definitive conclusions.

The benefit of using a longer data record can be demonstrated in the following student *t* tests. From the statistics point of view, the linear correlations obtained in Figures 4b, 4d, 5d–5f, and 9b–9d are the sample

Table 7
Comparison of Sample Correlations With Student t Test Values for Figures 4, 5, and 9

	Figure 4b	Figure 4d1	Figure 4d2	Figure 5d	Figure 5e	Figure 5f	Figure 9b	Figure 9c	Figure 9d
r	−0.77	−0.52	−0.75	0.85	0.77	0.65	−0.82	−0.76	0.6
P_r	0.999	0.85	0.97	~1	0.99995	0.9986	0.99	0.97	0.91
t	−1.6	−0.83	−1.5	4.2	3.2	2.3	−2.0	−1.6	1.0
P_t	0.87	0.75	0.87	0.998	0.992	0.972	0.90	0.87	0.79

correlation coefficients that are calculated from N samples. To draw conclusions about populations, the student t test for the hypothesis of population correlation $\rho = 0$ is given by

$$t = \frac{r - \rho}{\sqrt{(1 - r^2)/(n - 2)}} = \frac{r\sqrt{n - 2}}{\sqrt{1 - r^2}} \tag{5}$$

where r is the sample correlation coefficient and n is the effective degree of freedom. Here n is estimated, following Zülicke and Peters (2010), as the ratio of the observational time length over the persistent time of geophysical processes. In the case of this work, a typical QBO period is 28 months, and the observation time lengths are 108 and 252 months (i.e., 9 and 21 years) for lidar and MERRA-2 data sets, respectively. Assuming one QBO event is statistically independent from the other, the effective degree of freedom n is 3.86 and 9 for lidar observations and MERRA-2 data, respectively. Substitute n values into Equation 5, we compute the t values and confidence levels and compare them with the sample correlations in Table 7. In this table, r is the sample correlation coefficient, t is the student t test value, and P_r and P_t are the confidence levels of the sample and population correlations, calculated with N and n, respectively. The t values in Table 7 are far from 0, rejecting the hypothesis of $\rho = 0$. The confidence levels of population correlations are smaller than those of the corresponding sample correlations, but they are still convincing probabilities. The student t test results support the conclusions of the QBO signals in the gravity wave E_{pm} and the polar vortex edge location. Figures 5d–5f have the confidence levels well above 95% due to much larger effective degree of freedom ($n = 9$), while the probabilities for other figures are slightly below 95% due to the much smaller $n = 3.86$. If a longer data record enables $n = 6.4$ (e.g., 15 years of lidar observations), then the confidence level will be improved above 95%.

Other possible factors, such as tropospheric and stratospheric wave sources and the Doppler shifting effects as discussed in Chu et al. (2018), may also affect the interannual variations of gravity wave E_{pm} if these factors have long-term changes. Moreover, we make a few speculations here based on several interesting results from recent studies. (1) If the polar vortex acts as a barrier so that gravity waves cannot penetrate the vortex edge and propagate poleward from the midtropical/subtropical regions, the equatorward expansion of polar vortex edge will include larger areas within the polar vortex during QBOe than during QBOw, thereby more wave sources may be included, leading to higher chances for more waves to reach McMurdo. (2) Competing with this point is the finding made by Sato et al. (2009) that gravity waves propagating upward tend to focus on the axis of PNJ in the Antarctic winter season, and the focusing effect is largely dependent on the meridional gradient of the background zonal wind velocity (Hindley et al., 2019; Shibuya & Sato, 2019). The contraction of vortex area during QBOw will increase the meridional gradient of the zonal wind inside the polar vortex; thus, the focusing effects of GWs will become stronger during QBOw than during QBOe. The shorter distance from the PNJ to McMurdo and the more focusing of GWs into the PNJ may suggest higher E_{pm} over McMurdo during QBOw than during QBOe, seemingly controversial with the observations. (3) However, this gravity wave focusing effect may turn out to be supportive of the observations if we consider the case from another perspective. Results from recent high-resolution model simulations (Becker & Vadas, 2018; Vadas & Becker, 2018; Watanabe et al., 2006) indicate strong orographic gravity wave sources near McMurdo, which are attributed to the eastward downslope winds blowing down the steep slopes of the East Antarctic Plateau and Trans-Antarctic Mountains (altitudes over 4 km) onto the west coast of Ross sea. While some of these waves propagate to and focus into the axis of PNJ, the rest of these waves can propagate directly to McMurdo and other high-latitude locations (Vadas & Becker, 2018). If we consider that the midwinter PNJ location is far away from McMurdo (even in QBOw), the gravity waves focused into the axis of PNJ may not contribute much to the gravity waves over McMurdo. Then the less focusing effect during

QBOe means more chance for gravity waves to propagate to McMurdo from wave sources and thus possibly higher E_{pm} during QBOe as the lidar observed. Quantitative analyses of these factors, including the solar cycle and ENSO effects, and their contributions to the enhanced E_{pm} in the QBO easterly phase are beyond the scope of this work but will be addressed in future modeling studies.

7. Conclusions

Using 9 years of lidar observations (2011–2019) from McMurdo/Arrival Heights (77.84°S, 166.67°E), Antarctica, and 21 years of MERRA-2 reanalysis data (1999–2019), we present the first observations of potential QBO signals in the stratospheric gravity wave potential energy mass density (E_{pm}) at McMurdo and in the Antarctic polar vortex location near the stratopause. Midwinter stratospheric gravity wave activity is stronger during the QBO easterly years when the June polar vortex expands and the PNJ shifts equatorward. During the QBO westerly years, gravity wave activity is weaker when the polar vortex contracts and the PNJ moves poleward. The lidar-observed interannual variations of gravity wave E_{pm} winter maxima over McMurdo are most likely controlled by the equatorial QBO signals via modulating the polar vortex location and thus the critical level filtering of gravity waves in the Antarctic. The ENSO may play a minor role in modulating the E_{pm} interannual variations. The QBO signals in the polar vortex edge and PNJ during June months are robust and appear not to be affected by the solar cycle and ENSO to the first order.

In addition to the repeated seasonal pattern of summer minima and winter maxima, qualified lidar data of ~7,000 hr also exhibit interannual variations of gravity wave E_{pm} in the stratosphere 30–50 km. That is, the mean E_{pm} winter maxima in 2012, 2015, and 2018 (during QBOe) are ~43% higher than those in the other years (during QBOw). Using the 9-year composite-mean harmonic fit to represent the mean annual cycle, the McMurdo lidar observations reveal the positive/negative gravity wave E_{pm} anomalies during QBO easterly/westerly winters. The correlation of the E_{pm} anomaly with a QBO index averaged over the 40 and 50 hPa pressure levels reaches a coefficient of −0.766 with a confidence level of 99.9%, confirming a statistically significant correlation between the gravity wave E_{pm} and the QBO phase in the last decade. The positive E_{pm} anomalies occur when McMurdo is well inside the polar vortex core and the distance to the vortex edge is large; both of these aspects tend to occur during the QBO easterly winters.

Using the 21 years of MERRA-2 reanalysis data (1999–2019), we find that the June polar vortex edge near the stratopause moves equatorward/poleward during QBO easterly/westerly years. The correlation between the negative vortex edge distance from McMurdo at 45 km and a QBO index vertically averaged over 20, 30, 40, and 50 hPa pressure levels reaches a correlation coefficient of 0.846 with a confidence level of nearly 100%. The mean distance from McMurdo to the vortex edge, averaged over the QBO easterly years, reaches over 4,000 km, while the distance averaged over the QBO westerly years is about 3,000 km in June at 45 km. The mean wind along the vortex edge in June is weaker by 10–20 m/s in the QBO easterly than in the westerly years. Such vortex edge distance corresponds to the mean vortex edge near the stratopause (~50 km) located at 39.7°S and 47.7°S, respectively, for the QBO easterly and westerly phases. This latitude difference of ~8° is significant as it equates to a distance of nearly 1,000 km. The QBO signal in the polar vortex edge location is robust with statistical significance.

The equatorward shift of the PNJ core around the stratopause in the QBO easterly years and the poleward shift in the QBO westerly years are clear reflections of the vortex expansion/contraction during QBO easterly/westerly phases. The polar vortex edge is located along the poleward flank of the PNJ stream. During the QBO easterly phase, the polar vortex expands, pushing the PNJ toward the equator. The equatorward expansion of the polar vortex leads to quieter winters and more stable background winds during QBOe than QBOw and corresponds to less critical level filtering and thus higher E_{pm} in the upper stratosphere in the QBO easterly phase. The critical level filtering is characterized by the WRA, and our results support the hypothesis that the interannual variations of E_{pm} is mainly determined by the interannual variations of WRA, that is, the critical level filtering effects. WRA is likely modulated by the polar vortex location in the midwinter.

Why the SH polar vortex moves equatorward in QBOe, why the triple-cell structures are formed around the stratopause in the SH, and why gravity wave E_{pm} at McMurdo are enhanced in the QBOe when the polar vortex and PNJ move equatorward, are beyond the scope of this study. These intriguing questions deserve

future investigations with the combination of theories, models, and long-term observations. The underlying mechanisms may well reflect the asymmetry between two hemispheres and the complex atmospheric coupling from the equatorial to the polar regions. Furthermore, the QBO modulation of stratospheric gravity waves may impact the vertical wave coupling via modulating the generation of secondary gravity waves (Vadas et al., 2018) and wave dissipation altitudes (Vadas & Becker, 2019), which will affect persistent gravity waves in the MLT (Chen et al., 2016; Chu et al., 2018). It is likely to find QBO signals in the MLT, and such questions deserve future investigation using the lidar data collected from McMurdo. The observationally based study presented in this article lays the groundwork for future modeling studies that will test the observed relationships and proposed mechanisms in long-term climate simulations. Other future work will also investigate the roles of solar activity and ENSO as well as their entanglement with the QBO, polar vortex, and gravity waves.

Data Availability Statement

The data shown in this work can be downloaded online (from https://data.mendeley.com/datasets/96yhm3ct24/1).

Acknowledgments

We gratefully acknowledge the graduate students and research scientists who made contributions to the McMurdo lidar campaign, including winter-over lidar scientists Zhibin Yu (2011), Brendan Roberts (2012), Weichun Fong (2013), Cao Chen (2014), Jian Zhao (2015), Ian Barry (2016), Zhengyu Hua (2017), Dongming Chang (2018), Zimu Li and Ian Geraghty (2019), Xianxin Li and Cissi Lin (2020), and summer scientists Wentao Huang, Zhangjun Wang, John A. Smith, Xian Lu, Muzhou Lu, Clare Miller, and Jackson Jandreau. We are grateful to Richard Dean, Nikolas Sinkola, Adam Godfrey, Mark Murphy, Hue Tran, and Kate McKenzie for their engineering help and support. We thank Erich Becker and Sharon L. Vadas for intriguing discussions on orographic gravity waves and critical level filtering. We are indebted to Vladimir Papitashvili, Chester S. Gardner, and Adrian J. McDonald for their guidance and collaboration. We sincerely appreciate the staff of the United States Antarctic Program, McMurdo Station, Antarctica, New Zealand, and Scott Base for their superb support over the years. We gratefully acknowledge MERRA-2 data provided by the Global Modeling and Assimilation Office (GMAO) at NASA Goddard Space Flight Center through the NASA GES DISC online archive. This project was supported by the National Science Foundation (NSF) Grants OPP-0839091, OPP-1246405, and OPP-1443726. V. L. H. was supported by NASA HGI Grant NNX17AB80G and NASA HGR Grants 80NSSC18K1046 and 80NSSC19K0834. Xian Lu's research was supported by NSF Grants AGS-1705448 (CEDAR), OPP-1705450, and CAREER-1753214.

References

Alexander, M. J., Geller, M., McLandress, C., Polavarapu, S., Preusse, P., Sassi, F., et al. (2010). Recent developments in gravity-wave effects in climate models and the global distribution of gravity-wave momentum flux from observations and models. *Quarterly Journal of the Royal Meteorological Society*, *136*(650), 1103–1124. https://doi.org/10.1002/qj.637

Andrews, D. G., Holton, J. R., & Leovy, C. B. (1987). *Middle atmosphere dynamics* (). New York: Elsevier.

Anstey, J. A., & Shepherd, T. G. (2014). High-latitude influence of the Quasi-Biennial Oscillation. *Quarterly Journal of the Royal Meteorological Society*, *140*(678), 1–21. https://doi.org/10.1002/qj.2132

Baldwin, M. P., & Dunkerton, T. J. (1998). Quasi-biennial modulation of the Southern Hemisphere stratospheric polar vortex. *Geophysical Research Letters*, *25*(17), 3343–3346. https://doi.org/10.1029/98GL02445

Baldwin, M. P., Gray, L. J., Dunkerton, T. J., Hamilton, K., Haynes, P. H., Randel, W. J., et al. (2001). The Quasi-Biennial Oscillation. *Reviews of Geophysics*, *39*(2), 179–229. https://doi.org/10.1029/1999rg000073

Becker, E. (2012). Dynamical control of the middle atmosphere. *Space Science Reviews*, *168*(1-4), 283–314. https://doi.org/10.1007/s11214-011-9841-5

Becker, E. (2017). Mean-flow effects of thermal tides in the mesosphere and lower thermosphere. *Journal of the Atmospheric Sciences*, *74*(6), 2043–2063. https://doi.org/10.1175/jas-d-16-0194.1

Becker, E., & Vadas, S. L. (2018). Secondary gravity waves in the winter mesosphere: Results from a high-resolution global circulation model. *Journal of Geophysical Research: Atmospheres*, *123*, 2605–2627. https://doi.org/10.1002/2017jd027460

Bosilovich, M. G., Akella, S., Coy, L., Cullather, R., Draper, C., Gelaro, R., et al. (2015). MERRA-2: Initial evaluation of the ClimateRep. Greenbelt, MD: NASA.

Chen, C. (2016). Exploration of the mystery of polar wave dynamics with lidar/radar observations and general circulation models & development of new wave analysis methods (Doctoral Ddissertation). University of Colorado, Boulder, Boulder, Colorado.

Chen, C., & Chu, X. (2017). Two-dimensional Morlet wavelet transform and its application to wave recognition methodology of automatically extracting two-dimensional wave packets from lidar observations in Antarctica. *Journal of Atmospheric and Solar-Terrestrial Physics*, *162*, 28–47. https://doi.org/10.1016/j.jastp.2016.10.016

Chen, C., Chu, X., McDonald, A. J., Vadas, S. L., Yu, Z., Fong, W., & Lu, X. (2013). Inertia-gravity waves in Antarctica: A case study using simultaneous lidar and radar measurements at McMurdo/Scott Base (77.8°S, 166.7°E). *Journal of Geophysical Research: Atmospheres*, *118*, 2794–2808. https://doi.org/10.1002/jgrd.50318

Chen, C., Chu, X., Zhao, J., Roberts, B. R., Yu, Z., Fong, W., et al. (2016). Lidar observations of persistent gravity waves with periods of 3–10 h in the Antarctic middle and upper atmosphere at McMurdo (77.83°S, 166.67°E). *Journal of Geophysical Research: Space Physics*, *121*, 1483–1502. https://doi.org/10.1002/2015ja022127

Chu, X., Huang, W., Fong, W., Yu, Z., Wang, Z., Smith, J. A., & Gardner, C. S. (2011). First lidar observations of polar mesospheric clouds and Fe temperatures at McMurdo (77.8°S, 166.7°E), Antarctica. *Geophysical Research Letters*, *38*, L16810. https://doi.org/10.1029/2011GL048373

Chu, X., Pan, W., Papen, G. C., Gardner, C. S., & Gelbwachs, J. A. (2002). Fe Boltzmann temperature lidar: Design, error analysis, and initial results at the North and South Poles. *Applied Optics*, *41*(21), 4400–4410. https://doi.org/10.1364/AO.41.004400

Chu, X., & Yu, Z. (2017). Formation mechanisms of neutral Fe layers in the thermosphere at Antarctica studied with a thermosphere-ionosphere Fe/Fe^+ (TIFe) model. *Journal of Geophysical Research: Space Physics*, *122*, 6812–6848. https://doi.org/10.1002/2016ja023773

Chu, X., Yu, Z., Chen, C., Fong, W., Huang, W., & Gardner, C. S., et al. (2012). McMurdo lidar campaign: A new look into polar upper atmosphere. Paper presented at the 26th International Laser Radar Conference, Porto Heli, Greece.

Chu, X., Yu, Z., Fong, W., Chen, C., Zhao, J., Barry, I. F., et al. (2016). From Antarctica lidar discoveries to oasis exploration. *European Physical Journal Web of Conferences*, *119*, 12001. https://doi.org/10.1051/epjconf/201611912001

Chu, X., Yu, Z., Gardner, C. S., Chen, C., & Fong, W. (2011). Lidar observations of neutral Fe layers and fast gravity waves in the thermosphere (110–155 km) at McMurdo (77.8°S, 166.7°E), Antarctica. *Geophysical Research Letters*, *38*, L23807. https://doi.org/10.1029/2011GL050016

Chu, X., Zhao, J., Lu, X., Harvey, V. L., Jones, R. M., Becker, E., et al. (2018). Lidar observations of stratospheric gravity waves from 2011 to 2015 at McMurdo (77.84°S, 166.69°E), Antarctica: 2. Potential energy densities, lognormal distributions, and seasonal variations. *Journal of Geophysical Research: Atmospheres*, *123*, 7910–7934. https://doi.org/10.1029/2017JD027386

Coy, L., Wargan, K., Molod, A. M., McCarty, W. R., & Pawson, S. (2016). Structure and dynamics of the Quasi-Biennial Oscillation in MERRA-2. *Journal of Climate*, *29*(14), 5339–5354. https://doi.org/10.1175/jcli-d-15-0809.1

Fong, W., Lu, X., Chu, X., Fuller-Rowell, T. J., Yu, Z., Roberts, B. R., et al. (2014). Winter temperature tides from 30 to 110 km at McMurdo (77.8°S, 166.7°E), Antarctica: Lidar observations and comparisons with WAM. *Journal of Geophysical Research: Atmospheres*, *119*, 2846–2863. https://doi.org/10.1002/2013JD020784

Forbes, J. M. (1995). In R. M. Johnson, & T. L. Killeen (Eds.), *Tidal and planetary waves, in the upper mesosphere and lower thermosphere: A review of experiment and theory* (). Washington, DC: American Geophysical Union.

Ford, E. A. K., Hibbins, R. E., & Jarvis, M. J. (2009). QBO effects on Antarctic mesospheric winds and polar vortex dynamics. *Geophysical Research Letters*, *36*, L20801. https://doi.org/10.1029/2009GL039848

Fritts, D. C., & Alexander, M. J. (2003). Gravity wave dynamics and effects in the middle atmosphere. *Reviews of Geophysics*, *41*(1), 1003. https://doi.org/10.1029/2001RG000106

Fujiwara, M., Wright, J. S., Manney, G. L., Gray, L. J., Anstey, J., Birner, T., et al. (2017). Introduction to the SPARC Reanalysis Intercomparison Project (S-RIP) and overview of the reanalysis systems. *Atmospheric Chemistry and Physics*, *17*(2), 1417–1452. https://doi.org/10.5194/acp-17-1417-2017

Garcia, R. R., López-Puertas, M., Funke, B., Marsh, D. R., Kinnison, D. E., Smith, A. K., & González-Galindo, F. (2014). On the distribution of CO_2 and CO in the mesosphere and lower thermosphere. *Journal of Geophysical Research: Atmospheres*, *119*, 5700–5718. https://doi.org/10.1002/2013JD021208

Garcia, R. R., Smith, A. K., Kinnison, D. E., de la Cámara, Á., & Murphy, D. J. (2017). Modification of the gravity wave parameterization in the Whole Atmosphere Community Climate Model: Motivation and results. *Journal of the Atmospheric Sciences*, *74*(1), 275–291. https://doi.org/10.1175/JAS-D-16-0104.1

Gelaro, R., McCarty, W., Suárez, M. J., Todling, R., Molod, A., Takacs, L., et al. (2017). The Modern-Era Retrospective Analysis for Research and Applications, Version 2 (MERRA-2). *Journal of Climate*, *30*(14), 5419–5454. https://doi.org/10.1175/jcli-d-16-0758.1

Gelbwachs, J. A. (1994). Iron Boltzmann factor LIDAR: Proposed new remote-sensing technique for mesospheric temperature. *Applied Optics*, *33*(30), 7151–7156. https://doi.org/10.1364/AO.33.007151

Geller, M. A., Alexander, M. J., Love, P. T., Bacmeister, J., Ern, M., Hertzog, A., et al. (2013). A comparison between gravity wave momentum fluxes in observations and climate models. *Journal of Climate*, *26*(17), 6383–6405. https://doi.org/10.1175/jcli-d-12-00545.1

Harvey, V. L., Pierce, R. B., Fairlie, T. D., & Hitchman, M. H. (2002). A climatology of stratospheric polar vortices and anticyclones. *Journal of Geophysical Research*, *107*(D20), 4422. https://doi.org/10.1029/2001JD001471

Hauchecorne, A., & Chanin, M.-L. (1980). Density and temperature profiles obtained by lidar between 35 and 70 km. *Geophysical Research Letters*, *7*(8), 565–568. https://doi.org/10.1029/GL007i008p00565

Hindley, N. P., Wright, C. J., Smith, N. D., Hoffmann, L., Holt, L. A., Alexander, M. J., et al. (2019). Gravity waves in the winter stratosphere over the Southern Ocean: High-resolution satellite observations and 3-D spectral analysis. *Atmospheric Chemistry and Physics*, *19*(24), 15,377–15,414. https://doi.org/10.5194/acp-19-15377-2019

Hitchman, M. H., & Huesmann, A. S. (2009). Seasonal influence of the Quasi-Biennial Oscillation on stratospheric jets and Rossby wave breaking. *Journal of the Atmospheric Sciences*, *66*(4), 935–946. https://doi.org/10.1175/2008jas2631.1

Holton, J. R., & Tan, H.-C. (1980). The influence of the equatorial Quasi-Biennial Oscillation on the global circulation at 50 mb. *Journal of the Atmospheric Sciences*, *37*(10), 2200–2208. https://doi.org/10.1175/1520-0469(1980)037<2200:Tioteq>2.0.Co;2

Kim, Y. J., Eckermann, S. D., & Chun, H. Y. (2003). An overview of the past, present and future of gravity-wave drag parametrization for numerical climate and weather prediction models. *Atmosphere-Ocean*, *41*(1), 65–98. https://doi.org/10.3137/ao.410105

Labitzke, K. (1987). Sunspots, the QBO, and the stratospheric temperature in the north polar region. *Geophysical Research Letters*, *14*(5), 535–537. https://doi.org/10.1029/GL014i005p00535

Labitzke, K., & van Loon, H. (1988). Associations between the 11-year solar cycle, the QBO and the atmosphere. Part I: the troposphere and stratosphere in the northern hemisphere in winter. *Journal of Atmospheric and Terrestrial Physics*, *50*(3), 197–206. https://doi.org/10.1016/0021-9169(88)90068-2

Liu, H. (2019). Quantifying gravity wave forcing using scale invariance. *Nature Communications*, *10*, 2605. https://doi.org/10.1038/s41467-019-10527-z

Lu, X., Chu, X., Chen, C., Nguyen, V., & Smith, A. K. (2017). First observations of short-period eastward propagating planetary waves from the stratosphere to the lower thermosphere (110 km) in winter Antarctica. *Geophysical Research Letters*, *44*, 10,744–10,753. https://doi.org/10.1002/2017GL075641

Lu, X., Chu, X., Fong, W., Chen, C., Yu, Z., Roberts, B. R., & McDonald, A. J. (2015). Vertical evolution of potential energy density and vertical wave number spectrum of Antarctic gravity waves from 35 to 105 km at McMurdo (77.8°S, 166.7°E). *Journal of Geophysical Research: Atmospheres*, *120*, 2719–2737. https://doi.org/10.1002/2014JD022751

Lu, X., Chu, X., Fuller-Rowell, T., Chang, L., Fong, W., & Yu, Z. (2013). Eastward propagating planetary waves with periods of 1-5 days in the winter Antarctic stratosphere as revealed by MERRA and lidar. *Journal of Geophysical Research: Atmospheres*, *118*, 9565–9578. https://doi.org/10.1002/jgrd.50717

Lu, X., Wu, H., Chu, X., Oberheide, J., Mlynczak, M. G., & Russell, J. M. III (2019). Quasi-Biennial Oscillation of short-period planetary waves and polar night jet in winter Antarctica observed in SABER and MERRA-2 and mechanism study with a quasi-geostrophic model. *Geophysical Research Letters*, *46*, 13,526–13,534. https://doi.org/10.1029/2019GL084759

McLandress, C., Ward, W. E., Fomichev, V. I., Semeniuk, K., Beagley, S. R., McFarlane, N. A., & Shepherd, T. G. (2006). Large-scale dynamics of the mesosphere and lower thermosphere: An analysis using the extended Canadian Middle Atmosphere Model. *Journal of Geophysical Research*, *111*, D17111. https://doi.org/10.1029/2005JD006776

Meek, C. E., Manson, A. H., & Drummond, J. R. (2017). Comparison of Aura MLS stratospheric chemical gradients with north polar vortex edges calculated by two methods. *Advances in Space Research*, *60*(8), 1898–1904. https://doi.org/10.1016/j.asr.2017.06.009

Nash, E. R., Newman, P. A., Rosenfield, J. E., & Schoeberl, M. R. (1996). An objective determination of the polar vortex using Ertel's potential vorticity. *Journal of Geophysical Research*, *101*(D5), 9471–9478. https://doi.org/10.1029/96JD00066

Newman, P. A., Coy, L., Pawson, S., & Lait, L. R. (2016). The anomalous change in the QBO in 2015–2016. *Geophysical Research Letters*, *43*, 8791–8797. https://doi.org/10.1002/2016GL070373

Richter, J. H., Sassi, F., & Garcia, R. R. (2010). Toward a physically based gravity wave source parameterization in a general circulation model. *Journal of the Atmospheric Sciences*, *67*(1), 136–156. https://doi.org/10.1175/2009jas3112.1

Sato, K., Watanabe, S., Kawatani, Y., Tomikawa, Y., Miyazaki, K., & Takahashi, M. (2009). On the origins of mesospheric gravity waves. *Geophysical Research Letters*, *36*, L19801. https://doi.org/10.1029/2009GL039908

Shibuya, R., & Sato, K. (2019). A study of the dynamical characteristics of inertia-gravity waves in the Antarctic mesosphere combining the PANSY radar and a non-hydrostatic general circulation model. *Atmospheric Chemistry and Physics*, *19*(5), 3395–3415. https://doi.org/10.5194/acp-19-3395-2019

Smith, A. K. (2012a). Interactions between the lower, middle and upper atmosphere. *Space Science Reviews*, *168*(1-4), 1–21. https://doi.org/10.1007/s11214-011-9791-y

Smith, A. K. (2012b). Global dynamics of the MLT. *Surveys in Geophysics*, *33*(6), 1177–1230. https://doi.org/10.1007/s10712-012-9196-9

Smith, J. A., & Chu, X. (2015). High-efficiency receiver architecture for resonance-fluorescence and Doppler lidars. *Applied Optics*, *54*(11), 3173–3184. https://doi.org/10.1364/AO.54.003173

Triplett, C. C., Collins, R. L., Nielsen, K., Harvey, V. L., & Mizutani, K. (2017). Role of wind filtering and unbalanced flow generation in middle atmosphere gravity wave activity at Chatanika Alaska. *Atmosphere*, *8*(12), 27. https://doi.org/10.3390/atmos8020027

Vadas, S. L., & Becker, E. (2018). Numerical modeling of the excitation, propagation, and dissipation of primary and secondary gravity waves during wintertime at McMurdo Station in the Antarctic. *Journal of Geophysical Research: Atmospheres*, *123*, 9326–9369. https://doi.org/10.1029/2017JD027974

Vadas, S. L., & Becker, E. (2019). Numerical modeling of the generation of tertiary gravity waves in the mesosphere and thermosphere during strong mountain wave events over the southern Andes. *Journal of Geophysical Research: Space Physics*, *124*, 7687–7718. https://doi.org/10.1029/2019JA026694

Vadas, S. L., Fritts, D. C., & Alexander, M. J. (2003). Mechanism for the generation of secondary waves in wave breaking regions. *Journal of the Atmospheric Sciences*, *60*(1), 194–214. https://doi.org/10.1175/1520-0469(2003)060<0194:Mftgos>2.0.Co;2

Vadas, S. L., Zhao, J., Chu, X., & Becker, E. (2018). The excitation of secondary gravity waves from local body forces: Theory and observation. *Journal of Geophysical Research: Atmospheres*, *123*, 9296–9325. https://doi.org/10.1029/2017JD027970

van Loon, H., & Labitzke, K. (1994). The 10–12-year atmospheric oscillation. *Meteorologische Zeitschrift*, *3*(5), 259–266. https://doi.org/10.1127/metz/3/1994/259

Watanabe, S., Sato, K., & Takahashi, M. (2006). A general circulation model study of the orographic gravity waves over Antarctica excited by katabatic winds. *Journal of Geophysical Research*, *111*, D18104. https://doi.org/10.1029/2005JD006851

Yamashita, C., Chu, X., Liu, H.-L., Espy, P. J., Nott, G. J., & Huang, W. (2009). Stratospheric gravity wave characteristics and seasonal variations observed by lidar at the South Pole and Rothera, Antarctica. *Journal of Geophysical Research*, *114*, D12101. https://doi.org/10.1029/2008JD011472

Yamashita, Y., Naoe, H., Inoue, M., & Takahashi, M. (2018). Response of the Southern Hemisphere atmosphere to the stratospheric equatorial Quasi-Biennial Oscillation (QBO) from winter to early summer. *Journal of the Meteorological Society of Japan*, *96*(6), 587–600. https://doi.org/10.2151/jmsj.2018-057

Zhao, J., Chu, X., Chen, C., Lu, X., Fong, W., Yu, Z., et al. (2017). Lidar observations of stratospheric gravity waves from 2011 to 2015 at McMurdo (77.84°S, 166.69°E), Antarctica: 1. Vertical wavelengths, periods, and frequency and vertical wave number spectra. *Journal of Geophysical Research: Atmospheres*, *122*, 5041–5062. https://doi.org/10.1002/2016JD026368

Zülicke, C., & Peters, D. H. W. (2010). On the estimation of persistence in geophysical time series. *The European Physical Journal Special Topics*, *187*(1), 101–108. https://doi.org/10.1140/epjst/e2010-01275-2